NASA TM-84283

NASA Technical Memorandum 84283

NASA-TM-84283 19820025470

# Recent Applications of the Transonic Wing Analysis Computer Code TWING

N. R. Subramanian, Terry L. Holst, Scott D. Thomas

LIBRARY COPY

SEP 23 1982

LANGLEY RESEARCH CENTER
LIBRARY, NASA
HAMPTON, VIRGINIA

August 1982

NASA
National Aeronautics and
Space Administration

Dup.

```
                DISPLAY 11/6/1
        82N33346*#   ISSUE 24   PAGE 3385   CATEGORY 2  RPT#: NASA-TM-84283
        A-9035 NAS 1.15:84283   82/08/00  42 PAGES   UNCLASSIFIED DOCUMENT
  UTTL: Recent applications of the transonic wing analysis computer code, TWING
  AUTH: A/SUBRAMANIAN, N. R.;  B/HOLST, T. L.;  C/THOMAS, S. D.   PAA:
        C/(Informatics General Corp., Palo Alto, Calif.)
  CORP: National Aeronautics and Space Administration.  Ames Research Center,
        Moffett Field, Calif.    AVAIL.NTIS
  SAP:  HC A03/MF A01
  CIO:  UNITED STATES
  MAJS: /*COMPUTER PROGRAMS/*FACTORIZATION/*ITERATION/*LOW ASPECT RATIO WINGS/*
        TRANSONIC FLOW
  MINS: / AERODYNAMIC CONFIGURATIONS/ COMPARISON/ FIGHTER AIRCRAFT/ FINITE
        DIFFERENCE THEORY/ HIGH ASPECT RATIO/ TRANSPORT AIRCRAFT
  ABA:  R.J.F.




  ENTER:
```

NASA Technical Memorandum 84283

---

# Recent Applications of the Transonic Wing Analysis Computer Code TWING

---

N. R. Subramanian
Terry L. Holst, Ames Research Center, Moffett Field, California
Scott D. Thomas, Informatics General Corporation, Palo Alto, California

National Aeronautics and
Space Administration

**Ames Research Center**
Moffett Field, California 94035

N82-33467#
N-153,435

# RECENT APPLICATIONS OF THE TRANSONIC WING ANALYSIS COMPUTER CODE TWING

N. R. Subramanian,* Terry L. Holst and Scott D. Thomas†

Ames Research Center

## SUMMARY

This report presents an evaluation of the transonic-wing-analysis computer code TWING. TWING utilizes a fully implicit approximate factorization iteration scheme to solve the full potential equation in conservative form. A numerical elliptic-solver grid-generation scheme is used to generate the required finite-difference mesh. Several wing configurations have been analyzed, and the limits of applicability of the code have been evaluated. Comparisons of computed results have been made with available experimental data. Results indicate that the code is robust, accurate (when significant viscous effects are not present), and efficient. TWING generally produces solutions an order of magnitude faster than other conservative full potential codes using successive-line overrelaxation. The present method is applicable to a wide range of isolated wing configurations including high-aspect-ratio transport wings and low-aspect-ratio, high-sweep, fighter configurations.

## I. INTRODUCTION

Recently, computers have had an increasing role in the aerodynamic design of aircraft for transonic flight. The computation of three-dimensional transonic flows about wings in many senses has become a routine affair. However, currently available methods still are unable to accurately and efficiently predict transonic characteristics of wings with large variations in aspect ratio, Mach number, angle of attack, sweep, taper ratio, etc.

During recent years, inviscid transonic flow computations have been obtained using two formulations: (1) the transonic small disturbance (TSD) formulation and (2) the full potential (FP) formulation. The TSD formulation is valid for isentropic, irrotational flows involving thin bodies at small angles of attack and for transonic conditions. Flow-tangency boundary conditions are imposed on mean geometrical surfaces, for example, wing "slits" or fuselage "boxes." Thus, simplified grids can be used, usually involving sheared, stretched Cartesian coordinates. This is the primary reason why the TSD formulation was introduced before the FP formulation and why more complete geometrical configurations have been solved via the TSD approach.

The worst problem associated with the TSD formulation occurs at the wing leading edge where the stagnation region generally causes the small disturbance assumption to break down. However, this formulation yields results which are generally better than expected. Indeed, good correlations with experiment have been obtained for a wide variety of applications. Example applications using the TSD formulation can be found in references 1-5. Although the TSD formulation is capable of computing flows for relatively sophisticated geometries, the FP formulation is generally desired when an accurate solution near the wing leading edge is required.

---

*Senior NRC Associate.

†Research Scientist, Informatics General Corporation, Palo Alto, California.

The FP formulation is valid for isentropic, irrotational flows ranging from incompressible to transonic conditions. The flow-tangency boundary condition is prescribed in an exact manner (relative to the TSD approach) at the geometry surface. Thus a more complex mapping procedure is required with this approach. Example applications using the FP formulation can be found in references 6-10. In addition, a survey of computational transonic methods in which the TSD and FP formulations are compared and contrasted is presented in reference 11.

Recently, a large number of researchers have investigated various ways of improving solution convergence. This research direction has been largely necessitated by the slow rate of convergence associated with the standard relaxation algorithm, successive-line overrelaxation (SLOR). Some of the new algorithms investigated include multigrid (refs. 12-16), the strongly implicit procedure (SIP) (ref. 17), and various approximate factorization schemes (refs. 18-23).

In this study, the TWING computer code (transonic wing analysis) has been used to calculate the flow field around a variety of isolated wing geometries. The intent of this report is to provide a quantitative evaluation of this code with respect to reliability and accuracy in solving transonic-wing flow fields. This code uses the AF2 fully implicit approximate factorization scheme to solve the FP equation in conservative form (ref. 24). Supersonic regions of flow are stabilized in the spatial-differencing scheme by using an upwind bias in the density evaluation (refs. 19, 25, and 26). This causes the spatial differencing scheme to be first-order accurate in supersonic regions and second-order accurate in subsonic regions.

Variations in wing aspect ratio, taper ratio, sweep, twist, and airfoil cross section have all been investigated in the present study. General details of the TWING solution algorithm are discussed first, followed by detailed grid and flow-solver results. Correlations with experimental results are included for most of the cases presented.

## II. NUMERICAL ALGORITHM

### Governing Equations

The three-dimensional full-potential equation written in strong conservation-law form is given by

$$(\rho\phi_x)_x + (\rho\phi_y)_y + (\rho\phi_z)_z = 0 \qquad (1a)$$

$$\rho = \left[1 - \frac{\gamma - 1}{\gamma + 1}(\phi_x^2 + \phi_y^2 + \phi_z^2)\right]^{1/\gamma-1} \qquad (1b)$$

The density $\rho$ and velocity components $\phi_x$, $\phi_y$, and $\phi_z$, are nondimensionalized by the stagnation density $\rho_S$ and the critical sound speed $a_*$, respectively; x, y, and z are Cartesian coordinates in the streamwise, spanwise, and vertical directions, respectively, and $\gamma$ is the ratio of specific heats.

Equation (1) is transformed from the physical domain (Cartesian coordinates) to the computational domain by using a general independent variable transformation. This transformation (see fig. 1), indicated by

$$
\left.\begin{aligned}
\xi &= \xi(x,y,z) \\
\eta &= \eta(x,y,z) \\
\zeta &= \zeta(x,y,z)
\end{aligned}\right\} \tag{2}
$$

maintains the strong conservation-law form of equation (1) (see ref. 27). The full-potential equation written in the computational domain ($\xi - \eta - \zeta$ coordinate system) is given by

$$
\left(\frac{\rho U}{J}\right)_\xi + \left(\frac{\rho V}{J}\right)_\eta + \left(\frac{\rho W}{J}\right)_\zeta = 0 \tag{3a}
$$

$$
\rho = \left[1 - \frac{\gamma - 1}{\gamma + 1} (U\phi_\xi + V\phi_\eta + W\phi_\zeta)\right]^{1/\gamma-1} \tag{3b}
$$

where

$$
\left.\begin{aligned}
U &= A_1\phi_\xi + A_4\phi_\eta + A_5\phi_\zeta \\
V &= A_4\phi_\xi + A_2\phi_\eta + A_6\phi_\zeta \\
W &= A_5\phi_\xi + A_6\phi_\eta + A_3\phi_\zeta
\end{aligned}\right\} \tag{4a}
$$

$$
\left.\begin{aligned}
A_1 &= \xi_x^2 + \xi_y^2 + \xi_z^2 \\
A_2 &= \eta_x^2 + \eta_y^2 + \eta_z^2 \\
A_3 &= \zeta_x^2 + \zeta_y^2 + \zeta_z^2 \\
A_4 &= \xi_x\eta_x + \xi_y\eta_y + \xi_z\eta_z \\
A_5 &= \xi_x\zeta_x + \xi_y\zeta_y + \xi_z\zeta_z \\
A_6 &= \eta_x\zeta_x + \eta_y\zeta_y + \eta_z\zeta_z
\end{aligned}\right\} \tag{4b}
$$

and

$$
\left.\begin{aligned}
J &= \xi_x\eta_y\zeta_z + \xi_z\eta_x\zeta_y + \xi_y\eta_z\zeta_x \\
&\quad - \xi_z\eta_y\zeta_x - \xi_y\eta_x\zeta_z - \xi_x\eta_z\zeta_y \\
&= 1/(x_\xi y_\eta z_\zeta + x_\zeta y_\xi z_\eta + x_\eta y_\zeta z_\xi \\
&\quad - x_\xi y_\zeta z_\eta - x_\eta y_\xi z_\zeta - x_\zeta y_\eta z_\xi)
\end{aligned}\right\} \tag{5}
$$

Note that this formulation for the FP equation is more general than the formulation of reference 24. The simplification that all $\eta$ = constant surfaces coincide with $y$ = constant planes has been removed. Thus, completely general orientations of the $\xi - \eta - \zeta$ mesh can be supported with the present formulation. For more discussion on the details of this transformation procedure see reference 24.

## Grid Generation

The grid generation scheme used in the present three-dimensional formulation is a simple extension of the two-dimensional scheme presented in reference 28. The finite-difference mesh is generated using a standard two-dimensional algorithm. This requires solution of two Laplace equations in each spanwise plane used as a defining station. These equations are transformed to the computational domain and solved using a fast approximate-factorization relaxation algorithm (ref. 28).

This establishes values for $x$ and $z$ in each spanwise plane used as a defining station. Coordinate values ($x$ and $z$) for computational planes between the defining stations are obtained via linear interpolation. For the case of a wing with no taper or section variation, only two defining stations are required, one at the root and one outboard of the tip in the wing-extension region. The root station is user-specified, but the wing-extension station is always chosen as a flat plate. In addition, wing taper, twist, thickness, and sweep variations can be specified at each defining station.

The coordinate values in the spanwise direction ($y$ values) are computed from a stretching formula, that in its simplest form gives equal spacing over the wing with relatively rapid stretching beyond the tip. The $x$ and $z$ values generated for the first station outboard of the tip are used for each wing extension station. Then a smoothing step for the two $y$ = constant planes on either side of the tip is implemented to remove grid discontinuities, which may arise in the transition from an airfoil of positive thickness to one of zero thickness. An example grid generated using the procedure just discussed will be presented in the section on computed results.

## Spatial Differencing

A finite-difference approximation for equation (3) suitable for both subsonic and supersonic flow regions is given by

$$\overleftarrow{\delta}_\xi(\tilde{\rho}U/J)_{i+1/2,j,k} + \overleftarrow{\delta}_\eta(\bar{\rho}V/J)_{i,j+1/2,k} + \overleftarrow{\delta}_\zeta(\rho W/J)_{i,j,k+1/2} = 0 \tag{6}$$

where the operators $\overleftarrow{\delta}_\xi(\ )$, $\overleftarrow{\delta}_\eta(\ )$, and $\overleftarrow{\delta}_\zeta(\ )$ are first-order-accurate, backward-difference operators in the $\xi$, $\eta$, and $\zeta$ directions, respectively. The density coefficients $\tilde{\rho}$ and $\bar{\rho}$ are defined by

$$\left.\begin{aligned} \tilde{\rho}_{i+1/2,j,k} &= [(1-\nu)\rho]_{i+1/2,j,k} + \nu_{i+1/2,j,k}\,\rho_{i+r+1/2,j,k} \\ \bar{\rho}_{i,j+1/2,k} &= [(1-\nu)\rho]_{i,j+1/2,k} + \nu_{i,j+1/2,k}\,\rho_{i,j+s+1/2,k} \end{aligned}\right\} \tag{7}$$

where

$$\left.\begin{aligned} r &= \pm 1 \quad \text{when} \quad U_{i+1/2,j,k} \lessgtr 0 \\ s &= \pm 1 \quad \text{when} \quad V_{i,j+1/2,k} \lessgtr 0 \end{aligned}\right\} \tag{8}$$

and

$$\nu_{i+1/2,j,k} = \begin{cases} \max[(M^2_{i,j,k} - 1)C,0] & \text{for} \quad U_{i+1/2,j,k} > 0 \\ \max[(M^2_{i+1,j,k} - 1)C,0] & \text{for} \quad U_{i+1/2,j,k} < 0 \end{cases} \tag{9}$$

The quantity $M_{i,j,k}$ is the local Mach number, C is a user-specified constant (usually between 1.0 and 2.0); and the quantities U, V, and W are the contravariant velocity components computed using standard, second-order-accurate finite-difference formulas. The density $\rho$ is computed from the second-order-accurate discretized version of equation (3b) and is stored at half points in the finite-difference mesh (i.e., at $i+1/2,j,k$). Values needed at $i,j+1/2,k$ or $i,j,k+1/2$ are obtained using simple four-element averages.

The spatial differencing scheme given by equations (6-9) is centrally differenced and second-order accurate in subsonic regions. In supersonic regions, the differencing is a combination of (1) the second-order-accurate central differencing used in subsonic regions and (2) the first-order-accurate upwind differencing resulting from the upwind evaluation of the density coefficients ($\tilde{\rho}$ and $\bar{\rho}$). In the present formulation upwind evaluations of the density have been used along only the i and j indices (wraparound and spanwise directions, respectively). Thus the fully rotated form of the spatial difference scheme has not been used. This has not adversely affected convergence for any of the cases presented herein. However, other cases involving large regions of supersonic flow at the wing trailing edge may require the fully rotated difference scheme with all three values of density in equation (6) biased in the upwind direction.

## AF2 Iteration Scheme

The AF2 fully implicit iteration scheme used in the present study can be expressed in a three-step format given by

Step 1:

$$\left(\alpha - \frac{1}{A_k}\overrightarrow{\delta}_\eta A_j \overleftarrow{\delta}_\eta\right)g^n_{i,j} = \alpha\omega L\phi^n_{i,j,k} + \alpha A_{k+1} f^n_{i,j,k+1} \tag{10a}$$

Step 2:

$$\left(A_k \mp \beta_\xi \overset{\rightleftarrows}{\delta}_\xi - \frac{1}{\alpha}\overrightarrow{\delta}_\xi A_i \overleftarrow{\delta}_\xi\right)f^n_{i,j,k} = g^n_{i,j} \tag{10b}$$

Step 3:

$$(\alpha + \overleftarrow{\delta}_\zeta)C^n_{i,j,k} = f^n_{i,j,k} \tag{10c}$$

where the n superscript is an iteration index; $\alpha$ is an acceleration parameter; $L\phi^n_{i,j,k}$ is the nth iteration residual (defined by eq. (6)); $\omega$ is a relaxation factor, equal to 1.8 for all cases presented; $g^n_{i,j}$ is an intermediate result stored at each grid point in a given k plane; and $f^n_{i,j,k}$ is an intermediate result stored at each point in the finite-difference mesh. The $A_i$, $A_j$, and $A_k$, coefficients are defined by

$$\left.\begin{aligned} A_i &= (\tilde{\rho} A_1/J)^n_{i-1/2,j,k} \\ A_j &= (\bar{\rho} A_2/J)^n_{i,j-1/2,k} \\ A_k &= (\rho A_3/J)^n_{i,j,k-1/2} \end{aligned}\right\} \tag{11}$$

and the density coefficients $\tilde{\rho}$ and $\bar{\rho}$ are defined by equation (7).

The quantity $\alpha$ appearing in equation (10) can be considered as $\Delta t^{-1}$. The best choice for $\alpha$ is to use a sequence of values. The small values are particularly effective for reducing the low-frequency errors, and the large values are particularly effective for reducing the high-frequency errors. The $\alpha$ sequence given in reference 19 has been used for the computations presented herein.

A $\phi_{\xi t}$-type term has been added inside the brackets of step 2 (see eq. (10b)). This term is necessary to provide time-like damping to the iteration scheme. The parameter $\beta_\xi$ is user-specified and usually ranges between 0.05 and 0.3. Larger values are generally required for cases with larger regions of supersonic flow.

In step 1, the g array is obtained by solving a tridiagonal matrix equation for each $\xi$ = constant line in the kth plane. In step 2, the f array is obtained from g by solving a tridiagonal matrix equation for each $\eta$ = constant line, again for just the kth plane. Next, step 1 is used to obtain the g array for the k - 1 plane, and then step 2 is used to obtain the f array for the k - 1 plane, etc. This process continues until all values of f in the three-dimensional mesh are established. Then, by using step 3, the correction array is obtained from the f array by solving a simple bidiagonal matrix equation for each $\zeta$ line in the entire finite-difference mesh. Other aspects of the present spatial differencing and iteration schemes are discussed in more detail in reference 24.

## Boundary Conditions

The wing-surface boundary condition in the body-fitted coordinate system is implemented by applying

$$\left(\frac{\rho W}{J}\right)_{i,j,NK+1/2} = -\left(\frac{\rho W}{J}\right)_{i,j,NK-1/2} \tag{12}$$

where NK is the wing surface. A similar reflection condition is used for the symmetry plane (y = 0). Along the free stream and outer boundaries the initial free-stream distribution of $\phi$ is fixed for nonlifting conditions. For lifting wings the outer boundary is updated by the usual compressible vortex solution with circulation $\Gamma_j$. A user-specified relaxation parameter (RGAM) is used to control the circulation build up. Details describing the circulation algorithm can be found in reference 24.

# III. COMPUTED RESULTS

In this section several results computed from the TWING computer code are presented. In each case the solution procedure started with the numerical generation of the finite-difference mesh. An example grid is shown in figures 2-9 for the Wing C geometry obtained from reference 29 (configuration 4 in table 1). The $x/c$, $y/c$, and $z/c$ Cartesian coordinates used in these figures are based on an origin at the wing-root midchord and are normalized by root chord $c$. This grid contains $127 \times 27 \times 20 = 68{,}580$ points (wraparound, spanwise, and near-normal directions, respectively), and is typical of the grids used for the results presented herein. Note that with this grid $127 \times 17 = 2159$ points are used to define the wing surface geometry. This configuration is a high-sweep ($\Lambda_{LE} = 45°$), high-taper (TR = 0.3) wing with 8° of twist. The amount of taper and twist is apparent from figures 2, 3, and 4 which show blowups of the root, tip, and wing extension airfoil sections plotted to the same scale. Note the efficiency with which the "O mesh" topology clusters points around the airfoil-section geometry regardless of its position in the span (root or tip). For this particular grid a special clustering procedure has been used to cluster grid points at the wing leading edges. This is especially useful for wings with sharp leading edges. Figures 5 and 6 show additional detail about the wing root section leading and trailing edges, respectively. The wing planform including the surrounding mesh is shown in figure 7, and the grid in the $\xi$ = constant plane corresponding to the wing half-chord position (i.e., the wing on edge) is shown in figure 8. Apparent in these views is the wing-tip grid topology and the stretching rates used above and below the wing as well as outboard of the wing tip. Finally, figure 9 contains a perspective view of the three-dimensional grid which consists of the symmetry plane, wing surface and vortex-sheet grid distributions. This view very much represents the view of the wing mounted in the wind tunnel (except for the vortex sheet) and presents a good picture of the overall grid topology.

The first case presented consists of a large aspect ratio wing (AR = 40) with zero sweep. The airfoil section (Korn airfoil, see ref. 30) is constant in the spanwise direction. The freestream Mach number is 0.75 and the angle of attack is 0.115°. This case is basically two dimensional in nature (everywhere except at the tip) and, thus, is compared with the two-dimensional hodograph result of reference 30 in figure 10. The agreement for this transonic "shock free" case is quite good. The TWING code produces a small shock at the aft sonic line which is similar to other results produced for this sensitive problem (ref. 31).

The next case involves a subcritical calculation ($M_\infty = 0.7$, $\alpha = 4°$) about a moderately swept, tapered wing without twist (see conf. 1 in table 1). A comparison of wing surface pressures with experiment (ref. 32) is shown in figure 11. The computational angle of attack was set so as to approximately match the experimental value of lift rather than the experimental value of the angle of attack. This is primarily required to simulate viscous effects which are not modeled in the inviscid TWING formulation. Overall the agreement between the experiment and the computational result is excellent.

The next case involves the "Wing A" geometry of reference 29 (see also ref. 33). Characteristics of this high-taper, low-sweep wing are presented in table 1 (conf. 2). A comparison of wing surface pressures with experiment is shown in figure 12 for measured experimental conditions of $M_\infty = 0.818$, $\alpha = 2.9°$. Corrections to the experimental Mach number and angle of attack of -0.02 and -2.3° were required in the present computation (i.e., $M_{\infty,com} = 0.798$, and $\alpha_{com} = 0.6°$) to produce good correlation with the experimental pressure distributions. The wind tunnel wall-interference study conducted in reference 29 produced similar, but smaller corrections for this set of conditions ($\Delta M = -0.005$ and $\Delta\alpha = -1.4°$). The angle of attack correction of reference 29 was determined from the FLO 22 computer code (ref. 34) by varying the computational angle of attack until the computed upper and lower surface pressures in the wing leading edge region matched experiment. Then the difference between the experimental and computational angles of attack was taken as the desired angle of attack correction $\Delta\alpha$. After $\Delta\alpha$ was obtained, the Mach number correction ($\Delta M$) was determined by using the Bailey-Ballhaus TSD computer code (ref. 35). Experimentally measured wind-tunnel-wall pressures were imposed as boundary conditions on the outer boundary of the computational domain (set to model the wind-tunnel wall position). Next, free-air solutions were computed with variations in the Mach number to produce a "best match" free-air solution with the wind tunnel solution. The difference in Mach number (if sufficiently small) between the wind tunnel wall case and the "best match" free air case was taken to be $\Delta M$.

This wind tunnel correction procedure seems to be a good one as it includes nonlinear, three-dimensional effects, but could suffer from numerical uncertainties arising from viscous modeling as well as other numerical errors, for example, nonconservative differencing, mesh effects, etc. It should be noted that the corrections determined in reference 29 for the Wing A geometry, as well as other geometries to be discussed shortly, produced good agreement for comparisons between FLO22 and experiment, but not good agreement between other computer codes and experiment. The probable reason is that this correction procedure removes two types of errors: (1) wind-tunnel wall interference errors and (2) numerical errors associated with each computer code. This suggests that separate corrections tailored to each individual computer code may be required.

In the present case the increased angle of attack correction ($\Delta\alpha = -2.3°$) is probably the result of viscous effects but the discrepancy between the Mach number corrections is puzzling. At any rate, with the appropriate corrections, the present results are in good agreement everywhere except near the base of each shock outboard of the wing root where obvious shock/boundary layer interactions affect the local pressure distribution. The last pressure distribution at $y/c = 0.95$ is in only fair agreement with experiment and probably suffers from numerical modeling inadequacies at the tip.

The moderate sweep case presented in reference 29 (Wing B) is discussed next. See table 1 for specific characteristics of this geometry (conf. 3). Pressure coefficient comparisons with experiment are presented for Wing B at $M_\infty = 0.9$, and $\alpha = 3.9°$ (experimental conditions) in figure 13. The $\Delta M$ and $\Delta\alpha$ corrections used in the TWING results were -0.02 and -1.7°. The corresponding $\Delta M$ and $\Delta\alpha$ corrections computed in reference 29 were -0.005 and -1.0°. Overall, the agreement between experiment and TWING is good at every span station. The aft shock position near the root is about 5-10% too far downstream, but moves into good agreement outboard of the midchord position.

The last configuration presented from reference 29 is a high-sweep, low-aspect-ratio wing — Wing C. The characteristics of this geometry are presented in table 1 (conf. 4) and have already been displayed in figures 2-9 where several views of a sample grid about this configuration are presented. Three flow conditions for Wing C are considered in the present study: a weakly supercritical case, $M_\infty = 0.7$, $\alpha = 4.949°$; a moderately supercritical case, $M_\infty = 0.85$, $\alpha = 5.9°$ (design condition); and a strongly supercritical case $M_\infty = 0.9$, $\alpha = 4.914°$. Pressure distribution comparisons between the present computed results and experiment are shown for the first case in figure 14. For this case the experimental Mach number was matched and the angle of attack correction was -0.55°. Except for a slight overprediction of the minimum pressure at the leading-edge upper surface the overall agreement is excellent.

The second Wing C result is compared with experiment in figure 15. The Mach number and angle of attack corrections for this case are $\Delta M = -0.02$ and $\Delta\alpha = -0.9°$. The agreement for this case is quite good everywhere except at the tip where the need of viscous corrections is apparent. Of particular note in this calculation is the ability of the TWING code to predict the oblique shock which exists at both the third ($y/c = 0.5$) and fourth ($y/c = 0.7$) span stations. The differencing scheme in this region is entirely first-order accurate and yet little shock smearing is exhibited.

The final Wing C calculation ($M_\infty = 0.9$, $\alpha = 4.914°$) is compared with experiment in figure 16. For this case the numerically determined Mach number correction of reference 29 was $\Delta M = -0.01$, and the corresponding $\Delta M$ used in TWING was -0.02. Overall, the agreement between these results is good. Viscous effects probably cause the discrepancy in shock strength and position at the tip station ($y/c = 0.9$).

The experimental and computational spanwise load distributions for the three Wing C cases just presented are compared in figure 17. The agreement is best for the lower Mach number case and worsens somewhat for higher Mach numbers. This is probably due to the larger angle-of-attack corrections required for the higher Mach number cases to match the pressure distributions in a reasonable way. Nevertheless, the agreement is good in each case.

A convergence history for the last Wing C calculation is shown in figure 18. Both the lift and the number of supersonic points (NSP) plotted versus iteration number $n$, and computer time in seconds on the CRAY-1S computer are displayed. The lift and NSP levels are essentially established in about 20 iterations. After about 40 iterations the lift and NSP levels stabilize and the solution is essentially converged. More interesting is the amount of computer time required to establish the solution. The entire convergence history shown in figure 18 required only about 25 sec of computer time and the crudely converged solution (40 iterations) required about 13 sec. Solutions obtained with codes using the SLOR algorithm, similar meshes, and the same computer would require at least an order of magnitude more computer time to achieve a similar level of convergence.

The small amount of computer time required per iteration, which is just as important as the small number of iterations required for a solution, is caused by several factors. The first is the high speed of the CRAY-1S computer. Second, the small number of operations packed into the fully implicit AF2 iteration scheme represents a minimum burden to any computer. Last, and most important, the way in which the operations of the AF2 iteration scheme lend themselves to efficient vector processing greatly speeds the computational processing rate within the TWING computer code. Other algorithms, such as SLOR, would not be so efficiently vectorized because of inherently recursive operations.

To obtain an idea of the effects of the angle of attack ($\Delta\alpha$) and Mach number ($\Delta M$) corrections discussed earlier, several pertinent results are shown in figure 19. The pressure coefficient distributions at two span stations for configuration 4 ($\eta \sim 0.30$ and 0.70) are compared with experiment for several conditions: (1) the uncorrected experimental conditions ($M_\infty = 0.85$, $\alpha = 5.9°$), (2) the corrected experimental conditions using the corrections cited in reference 29 ($M_\infty = 0.845$, $\alpha = 5.0°$), and (3) the corrected experimental conditions using the present corrections ($M_\infty = 0.83$, $\alpha = 5.0°$). As seen from figure 19 the angle of attack correction is more important than the Mach number correction. The conditions cited in reference 29 yield a reasonable solution in the present case, primarily because both angle-of-attack corrections are the same.

The next two numerical/experimental correlations are for the ATFI (Advanced Technology Fighter Integration) configuration obtained from General Dynamics-Fort Worth (R. Cox, private communication, 1982). Details of this configuration are given in table 1 (conf. 5). This geometry is a high-sweep, low-aspect-ratio wing with an unusually small taper ratio (TR = 0.177). Such a TR places heavy demands on the numerical scheme because of the highly sheared mesh which results. Two flow conditions are considered for this configuration: (1) $M_\infty = 0.6$, $\alpha = 3.99°$ and (2) $M_\infty = 0.9$, $\alpha = 4.01°$. Pressure coefficient comparisons for the first case are presented in figure 20. Excellent agreement with experiment is obtained for this subcritical case everywhere except at the tip (y/c = 0.897) where the tip missile used in the experiment was not modeled in the numerical simulation. The sharp-leading edge expansion predicted in the numerical result on the upper surface actually extends beyond the plotted results shown in figure 20 to a peak value of $C_p \sim -2.7$. It has been truncated to provide a more accurate scale for the rest of the $C_p$ distribution shown at each spanwise station. Repeated refinements of the mesh in the leading edge region indicate that the peak is numerically correct and indeed, a similar peak, although much smaller in extent, is exhibited at several span stations in the experiment. It is anticipated that viscous effects and/or pressure tap averaging effects are responsible for the mismatch between the peak levels.

The last ATFI solution considered is an extremely difficult case consisting of a freestream Mach number of 0.9 and 4° angle of attack. A comparison between numerical and experimental results is shown in figure 21. Except for expected discrepancies at the shocks, trailing edge, and tip (because of the absence of the experimentally mounted tip missile) the agreement is remarkably good. The leading edge expansion/shock and the aft shock details are accurately predicted at each span station away from the tip.

Figures 22 and 23 present the results of an interesting study to determine the ability of TWING to handle both positive and negative sweep. The shock sonic line has been plotted in each figure on a normalized planform of the wing. This configuration consisted of a parallelogram NACA 0012 wing (i.e., TR = 1.0) at $M_\infty = 0.8$, $\alpha = 3°$. The aspect ratio was six. Figure 22 shows results for positive, or aft, sweep (sweep = 0°, 20°, 30°, 50°, and 60°), and figure 23 shows results for negative, or forward, sweep (sweep = 0°, -20°, -30°, -50°, -60°, and -70°). A case involving +70° of sweep was also obtained, but because it was entirely subcritical, no result at $\Lambda = 70°$ appears in figure 22. As expected, the shock position moves forward and decreases in strength for increasing sweep (either positive or negative). For all cases the shock approaches the symmetry plane wall (2y/b = 0) in a normal fashion (i.e., in the physical domain), as it must to satisfy inviscid tangent-flow boundary conditions. This causes the variation in position of the shock/symmetry-plane intersection as shown in figures 22 and 23.

Of particular interest in these calculations is the robustness displayed by the TWING code. The TWING grid mapping becomes singular as the sweep angle approaches 90°. In addition, cross-derivative terms in the transformed FP equation grow as the sweep increases. Since these cross-derivative terms are not represented in an implicit fashion in the AF2 iteration scheme, instability might be expected to develop for even moderate levels of sweep. However, as indicated by the present results very large values of sweep ($-70° \leq \Lambda \leq 70°$) can be accommodated by the TWING computer code in a stable fashion.

A summary of computer times obtained from the TWING computer code for a range of computed examples is shown in table 2. The convergence for each of these cases is generally nonoptimal. The iteration number corresponds to the number of iterations required to reduce the initial maximum residual by two orders of magnitude. Computation times based on this measure of convergence range from 28 sec to 67 sec. Essentially converged results are obtained when the lift is bounded by a 2% band about the final value of lift. This level of convergence yields computational times ranging from 13 sec to 43 sec. The grid generation time is also displayed and ranges from 1.3 sec (three defining stations) to 3.0 sec (five defining stations).

These computational times are generally an order of magnitude smaller than other conservative full potential codes using SLOR on the same computer (see ref. 24 for a comparison between FLO28 and TWING). In addition, the advantage of vectorization, as provided by the CRAY-1S vector computer, produces over an order of magnitude improvement in computational speed for TWING relative to the slower CDC 7600 computer (see ref. 36 for more discussion on this point).

## IV. CONCLUSIONS

The TWING three-dimensional transonic full-potential computer program has been evaluated using a wide range of test examples. Calculated pressure distributions have been compared with experiment for most of the cases presented. The major conclusions of this study are as follows:

(1) Good correlation with experimental pressure distributions have been obtained in generally all cases when viscous effects were not important (that is, when strong shocks and the associated shock/boundary layer interaction effects are not present).

(2) The TWING computer program has proven to be computationally efficient (even without optimizing each individual run for minimum run time) and robust (no convergence problems were encountered for the cases presented herein).

(3) The TWING computer program has proven to be geometrically general for isolated-wing calculations in that a wide range of geometries has been run including high-aspect-ratio, low-taper transport-type configurations and low-aspect-ratio, high-taper fighter-type configurations.

(4) Viscous effects need to be introduced to model shock/boundary-layer interactions, decambering and displacement thickness effects, and trailing-edge separation and wake effects.

# V. REFERENCES

1. Mason, W.; Mackenzie, D. A.; Stern, M. A.; and Johnson, J. K.: A Numerical Three-Dimensional Viscous Transonic Wing-Body Analysis and Design Tool. AIAA Paper 78-101, Jan. 1978.

2. Albone, C. M.; Hall, M. G.; and Joyce, G.: Numerical Solutions for Transonic Flows Past Wing-Body Configurations. Symposium Transsonicum II, Gottingen, Sept. 1975, Springer-Verlag, 1976.

3. Boppe, C. W.; and Stern, M. A.: Simulated Transonic Flows for Aircraft with Nacelles, Pylons, and Winglets. AIAA Paper 80-130, Jan. 1980.

4. van der Vooren, J.; Slooff, J. W.; Huizing, G. H.; and van Essen, A.: Remarks on the Suitability of Various Transonic Small Perturbation Equations to Describe Three-Dimensional Transonic Flow; Examples of Computations Using a Fully-Conservative Rotated Difference Scheme. Symposium Transsonicum II, Gottingen, Sept. 1975, Springer-Verlag, 1978.

5. Wai, J. C.; Yoshihara, H.; and Abeyounis, W. K.: Transonic Perturbation Analysis of Wing-Fuselage-Nacelle-Pylon Configurations with Powered Jet Exhausts. AIAA Paper 82-0255, Jan. 1982.

6. Jameson, A.: Iterative Solution of Transonic Flows Over Airfoils and Wings, Including Flows at Mach 1. Comm. on Pure and Applied Math, vol. 27, 1974, pp. 283-309.

7. Caughey, D. A.; and Jameson, A.: Numerical Calculation of Transonic Potential Flow About Wing-Body Combinations. AIAA J., vol. 17, no. 2, Feb. 1979, pp. 175-181.

8. Caughey, D. A.; and Jameson, A.: Progress in Finite-Volume Calculations for Wing-Fuselage Combinations. AIAA J., Nov. 1980, pp. 1281-1288.

9. Chattot, J. J.; Coulombeix, C.; and da Silva Tome, C.: Calculs d'ecoulements Transsoniques Autour d'ailes. La Recherche Aerospatiale, no. 4, 1978, pp. 143-159.

10. Yu, N. J.: Transonic Flow Simulations for Complex Configurations with Surface Fitted Grids. AIAA Paper 81-1258, June 1981.

11. Holst, T. L.; Slooff, J. W.; Yoshihara, H.; and Ballhaus, Jr., W. F.: Applied Computational Transonic Aerodynamics. AGARDograph in print, 1982.

12. Jameson, A.: Acceleration of Transonic Potential Flow Calculations on Arbitrary Meshes by the Multiple Grid Method. AIAA Paper 79-1458, July 1979.

13. McCarthy, D. R.; and Reyhner, T. A.: A Multi-Grid Code for Three-Dimensional Potential Flow About Axisymmetric Inlets at Angle of Attack. AIAA Paper 80-1365, July 1980.

14. Shmilovich, A.; and Caughey, D. A.: Application of the Multi-Grid Method to Calculations of Transonic Potential Flow About Wing-Fuselage Combinations. NASA CP-2202, 1981.

15. Boerstoel, J. W.: A Multi-Grid Algorithm for Steady Transonic Potential Flows Around Aerofoils Using Newton Iteration. NASA CP-2202, 1981.

16. Deconinck, H.; and Hirsch, C.: A Multigrid Method for the Transonic Full Potential Equation Discretized with Finite Elements on an Arbitrary Body Fitted Mesh. NASA CP-2202, 1981.

17. Sankar, N. L.; Malone, J. B.; and Tassa, Y.: An Implicit Conservative Algorithm for Steady and Unsteady Three-Dimensional Transonic Potential Flows. Proceedings of the AIAA 5th CFD Conf., Palo Alto, Calif., June 1981.

18. Ballhaus, Jr., W. F.; Jameson, A.; and Albert, J.: Implicit Approximate Factorization Schemes for the Efficient Solution of Steady Transonic Flow Problems. AIAA J., vol. 16, 1978, pp. 573-579.

19. Holst, T. L.; and Ballhaus, Jr., W. F.: Fast Conservative Schemes for the Full Potential Equation Applied to Transonic Flows. AIAA J., vol. 17, no. 2, Feb. 1979, pp. 145-152.

20. Holst, T. L.: A Fast, Conservative Algorithm for Solving the Transonic Full-Potential Equation. AIAA J., vol. 18, no. 12, Dec. 1980, pp. 1431-1439.

21. Baker, T. J.: Potential Flow Calculation by the Approximate Factorization Method. J. of Comp. Phys., vol. 42, 1981, pp. 1-19.

22. Baker, T. J.; and Forsey, C. R.: A Fast Algorithm for the Calculation of Transonic Flow Over Wing/Body Combinations. Proceedings of the AIAA 5th CFD Conf., Palo Alto, Calif., June 1981.

23. Benek, J.; Steinhoff, J.; and Jameson, A.: Application of Approximate Factorization to Three-Dimensional Transonic Potential Flow Calculations. Presented at the AIAA 5th CFD Conf., Palo Alto, Calif., June 1981.

24. Holst, T. L.; and Thomas, S. D.: Numerical Solution of Transonic Wing Flow Fields. AIAA Paper 82-0105, Jan. 1982.

25. Hafez, M.; South, J.; and Murman, E.: Artificial Compressibility Methods for Numerical Solutions of Transonic Full Potential Equation. AIAA J., vol. 17, no. 8, Aug. 1979, pp. 838-844.

26. Eberle, A.: A Finite Volume Method for Calculating Transonic Potential Flow Around Wings from the Pressure Minimum Integral. NASA TM-75324, Translated from MBB UFE 1407(0), Feb. 1978.

27. Steger, J. L.: Implicit Finite Difference Simulation of Flow About Arbitrary Geometries with Application to Airfoils. AIAA J., vol. 16, July 1978, pp. 679-686.

28. Holst, T. L.: An Implicit Algorithm for the Conservative, Transonic Full Potential Equation Using an Arbitrary Mesh. AIAA J., vol. 17, Oct. 1979, pp. 1038-1045.

29. Hinson, B. L.; and Burdges, K. P.: Acquisition and Application of Transonic Wing and Far-Field Test Data for Three-Dimensional Computational Method Evaluation. AFSOR-TR-80-0421, March 1980.

30. Bauer, F.; Garabedian, P.; Korn, D.; and Jameson A.: Supercritical Wing Sections II. Vol. 108, Springer-Verlag, New York, 1975.

31. Jameson, A.: Transonic Flow Calculations. VKI Lecture Series no. 87, March 1976.

32. Edwards, G. G.; and Boltz, F. W.: An Analysis of the Forces and Pressure Distribution on a Wing with the Leading Edge Swept Back 37.25 deg. NACA RM A9K01, March 1950.

33. Hinson, B. L.; and Burdges, K. P.: An Evaluation of Three-Dimensional Transonic Codes Using New Correlation-Tailored Test Data. AIAA Paper 80-0003, Jan. 1980.

34. Jameson, A.; and Caughey, D. A.: Numerical Calculation of the Transonic Flow Past a Swept Wing. COO-3077-140, ERDA Math. and Comput. Lab., New York Univ., June 1977 (also available as NASA CR-153297).

35. Ballhaus, Jr., W. F.; Bailey, F. R.; and Frick, J.: Improved Computational Treatment of Transonic Flow About Swept Wings. NASA CP-2001, Nov. 1976.

36. Thomas, S. D.; and Holst, T. L.: Numerical Computation of Transonic Flow About Wing-Fuselage Configurations on a Vector Computer. Paper submitted to the AIAA 21st Aerospace Sciences Meeting, Reno, Nevada, Jan. 1983.

TABLE 1.- SELECTED WING GEOMETRY PARAMETERS

| | Configuration 1 (ref. 32) | Configuration 2 (ref. 29) | Configuration 3 (ref. 29) | Configuration 4 (ref. 29) | Configuration 5 [a] |
|---|---|---|---|---|---|
| Aspect ratio (Æ) | 6.0 | 8.0 | 3.8 | 2.6 | 3.8 |
| Taper ratio (TR) | .5 | .4 | .4 | .3 | .177 |
| Leading edge sweep ($\Lambda_{LE}$) | 37.25 | 27 | 35 | 45 | 40 |
| Root angle of attack $\theta_r$ ~ deg | 0 | 2.76 | 2.50 | 2.38 | 0 |
| Tip angle of attack $\theta_t$ ~ deg | 0 | -2.04 | -4.00 | -5.79 | 3.0 |
| Root thickness-to-chord ratio $(t/c)_r$ | .12 | .12 | .06 | .07 | .04 |
| Tip thickness-to-chord ratio $(t/c)_t$ | .12 | .12 | .06 | .11 | .04 |

[a] R. Cox, private communication, 1982.

TABLE 2.- TWING CONVERGENCE TIMES ON THE CRAY-1S COMPUTER (NONOPTIMAL CONVERGENCE), ALL TIMES ARE FOR A 127×27×20 (68580) MESH WITH 127×17 (2159) SURFACE MESH POINTS

| Wing | $M_\infty$ | $\alpha_w$, deg | CPU time grid generation, sec | Number of iterations | CPU time, sec | CPU time for 98% development of lift, sec |
|---|---|---|---|---|---|---|
| Configuration | | | | | | |
| 2 | 0.798 | 0.6 | 1.3 | 164 | 51.8 | 31.0 |
| 3 | .88 | 2.2 | 1.3 | 170 | 54.9 | 12.9 |
| 4 | .7 | 4.4 | 1.4 | 90 | 27.6 | 17.2 |
| 4 | .83 | 5.0 | 1.4 | 99 | 30.9 | 18.1 |
| 4 | .88 | 3.8 | 1.4 | 83 | 28.9 | 14.3 |
| 5 | .6 | 3.5 | 3.0 | 102 | 31.3 | 18.7 |
| 5 | .9 | 3.0 | 3.0 | 196 | 66.8 | 43.0 |

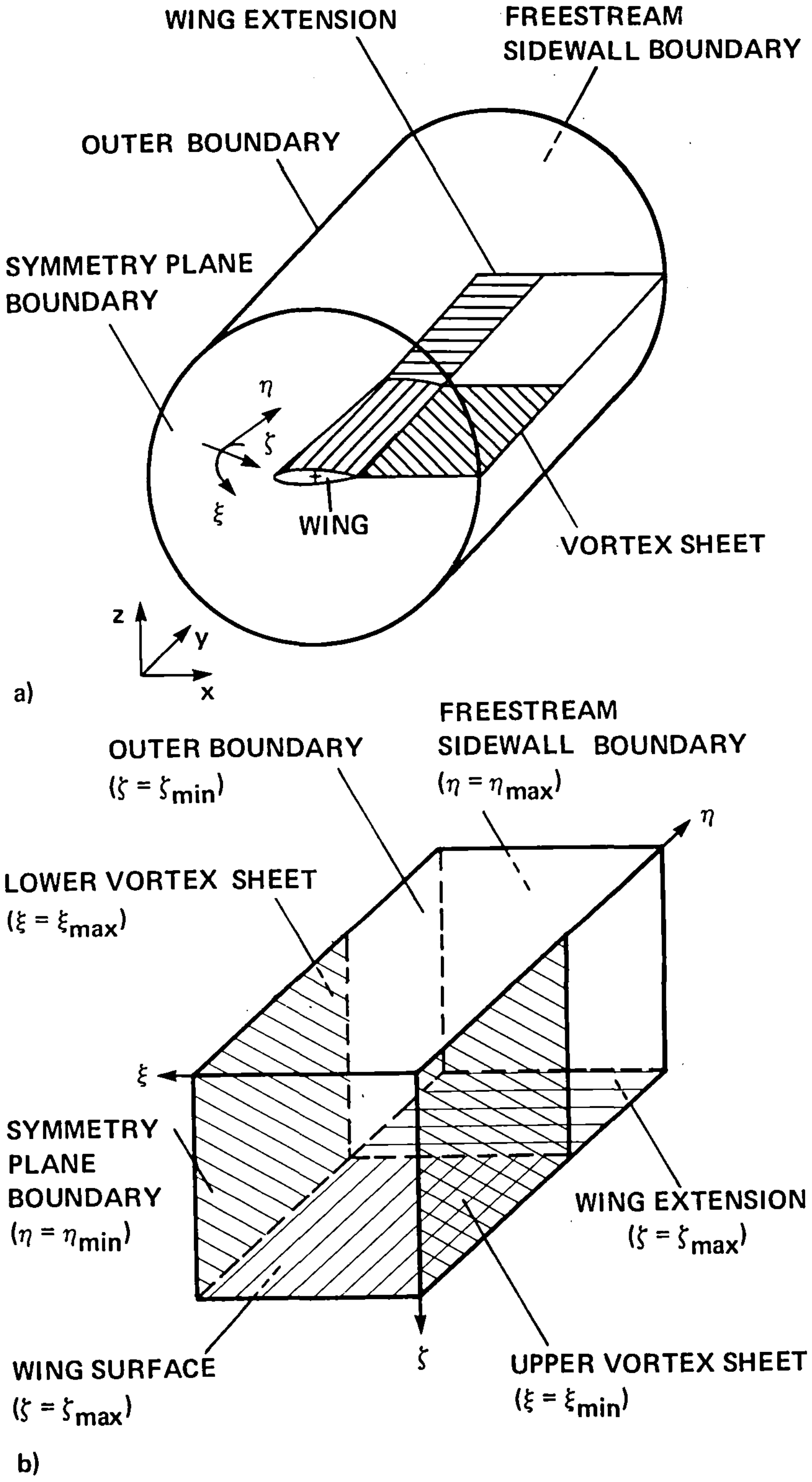
WING EXTENSION
FREESTREAM SIDEWALL BOUNDARY
OUTER BOUNDARY
SYMMETRY PLANE BOUNDARY
η
ζ
ξ
WING
VORTEX SHEET
z
y
x
a)
OUTER BOUNDARY (ζ = ζmin)
FREESTREAM SIDEWALL BOUNDARY (η = ηmax)
η
LOWER VORTEX SHEET (ξ = ξmax)
ξ
SYMMETRY PLANE BOUNDARY (η = ηmin)
WING EXTENSION (ζ = ζmax)
WING SURFACE (ζ = ζmax)
ζ
UPPER VORTEX SHEET (ξ = ξmin)
b)

Figure 1.- Schematic of general $(x,y,z) \leftrightarrow (\xi,\eta,\zeta)$ transformation: a) physical domain, b) computational domain.

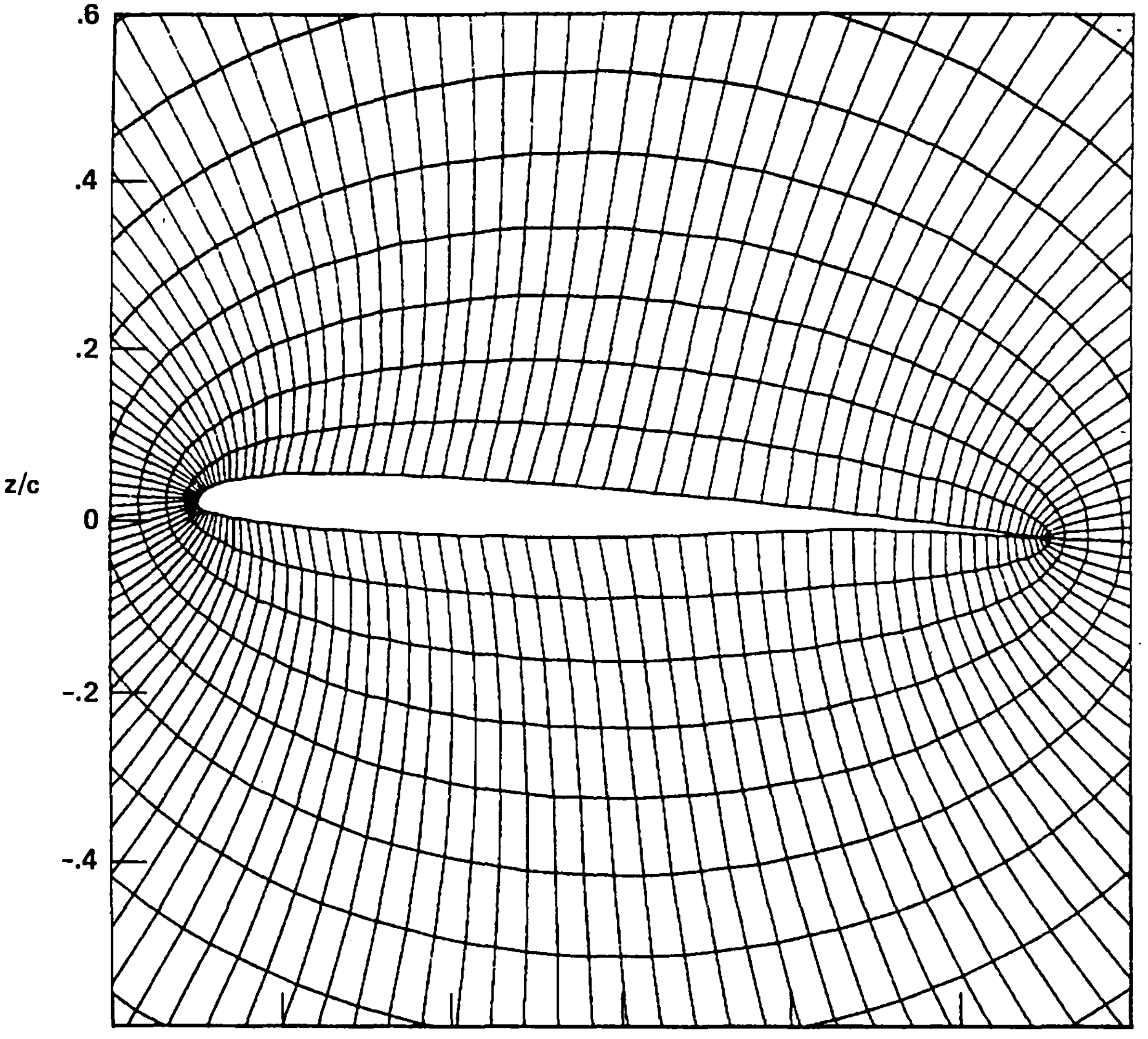
.6
.4
.2
z/c
0
-.2
-.4
-.6
-.4
-.2
0
.2
.4
.6
x/c

Figure 2.- Numerically generated finite-difference mesh about configuration 4 (ref. 29), root station (127×20 grid points).

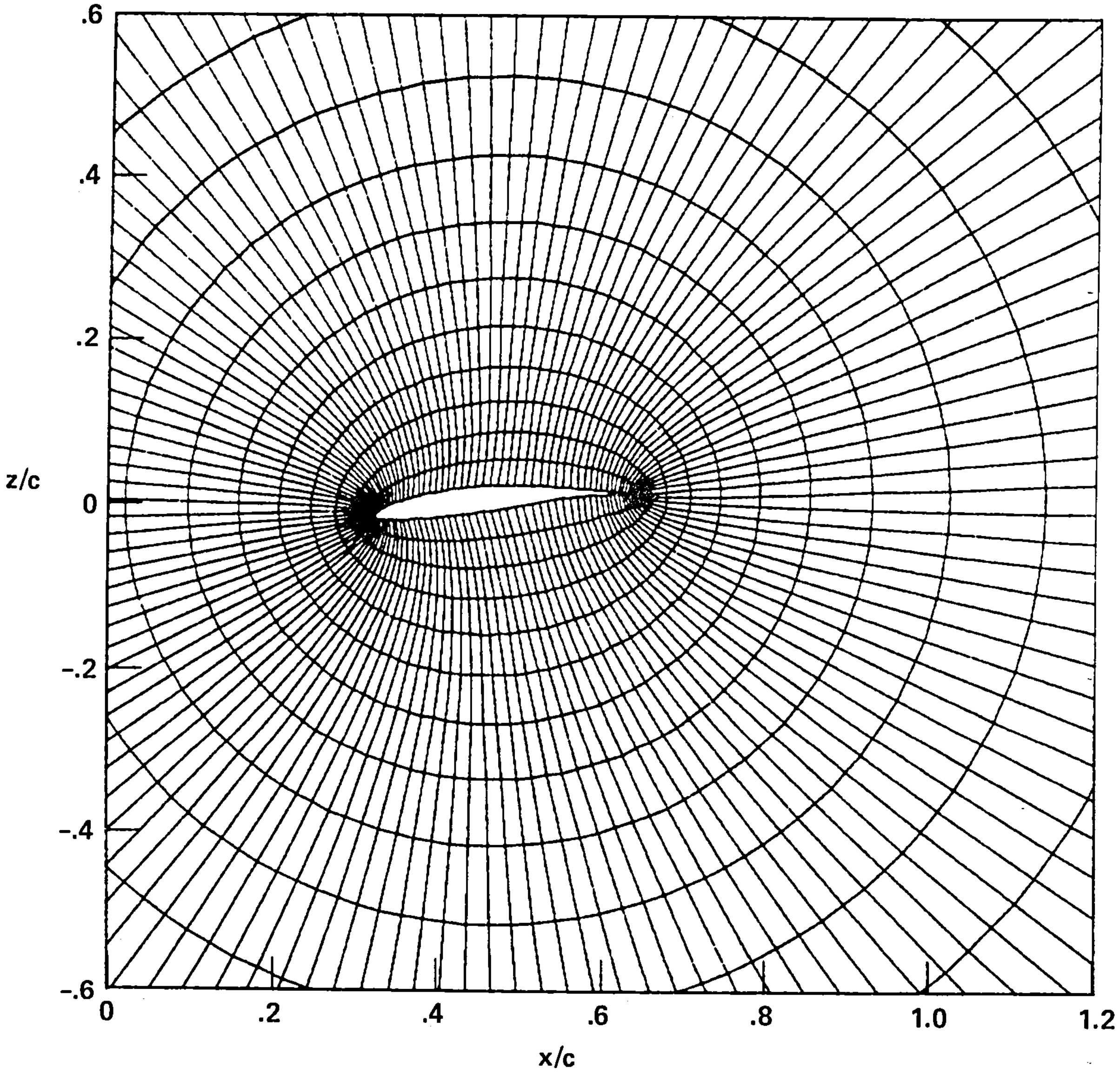
.6
.4
.2
z/c
0
-.2
-.4
-.6
0
.2
.4
.6
.8
1.0
1.2
x/c

Figure 3.- Numerically generated finite-difference mesh about configuration 4 (ref. 29), tip station (127×20 grid points).

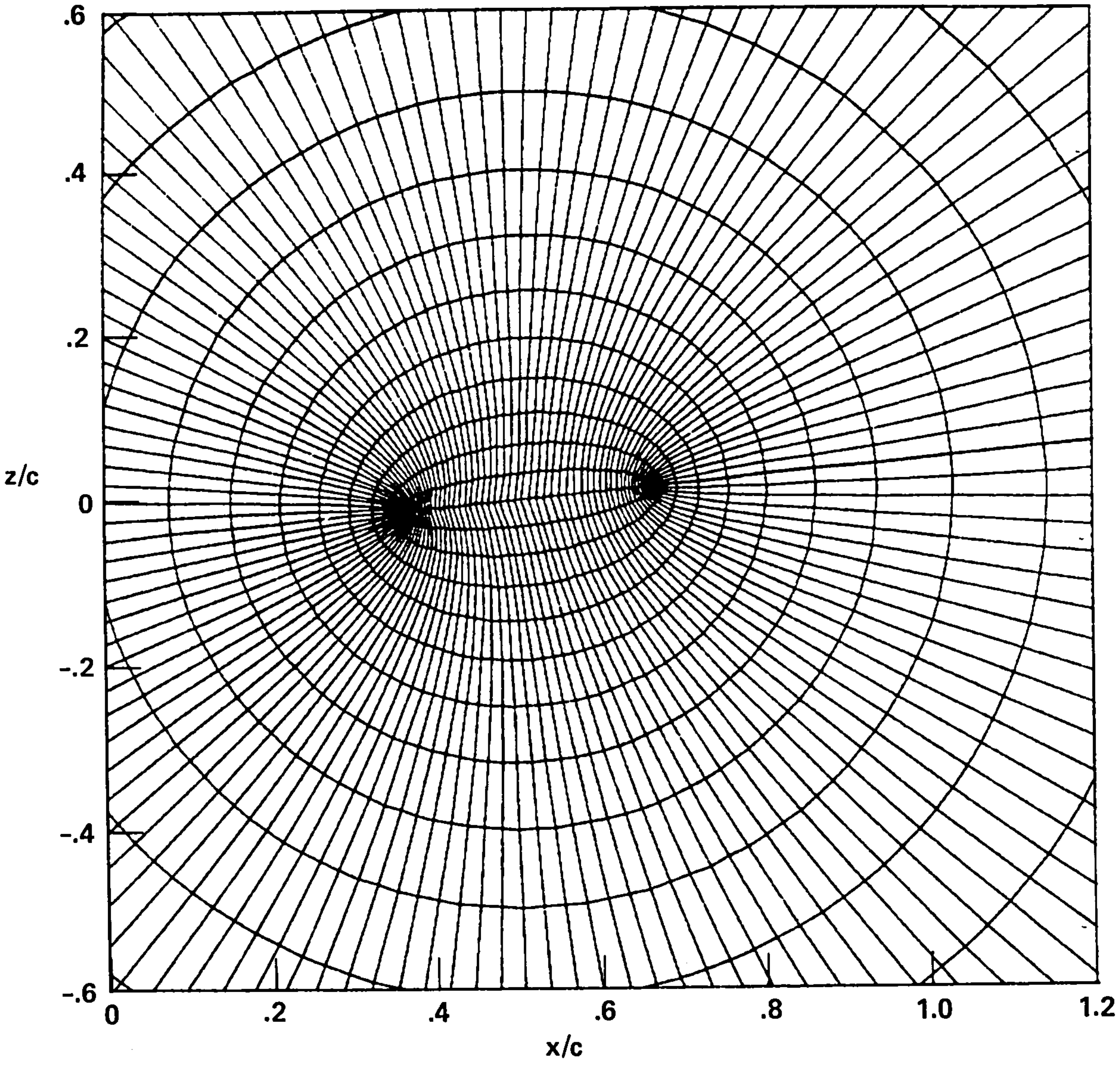

.6
.4
.2
z/c
0
-.2
-.4
-.6
0
.2
.4
.6
.8
1.0
1.2
x/c

Figure 4.- Numerically generated finite-difference mesh about configuration 4 (ref. 29), station outboard of the tip (127×20 grid points).

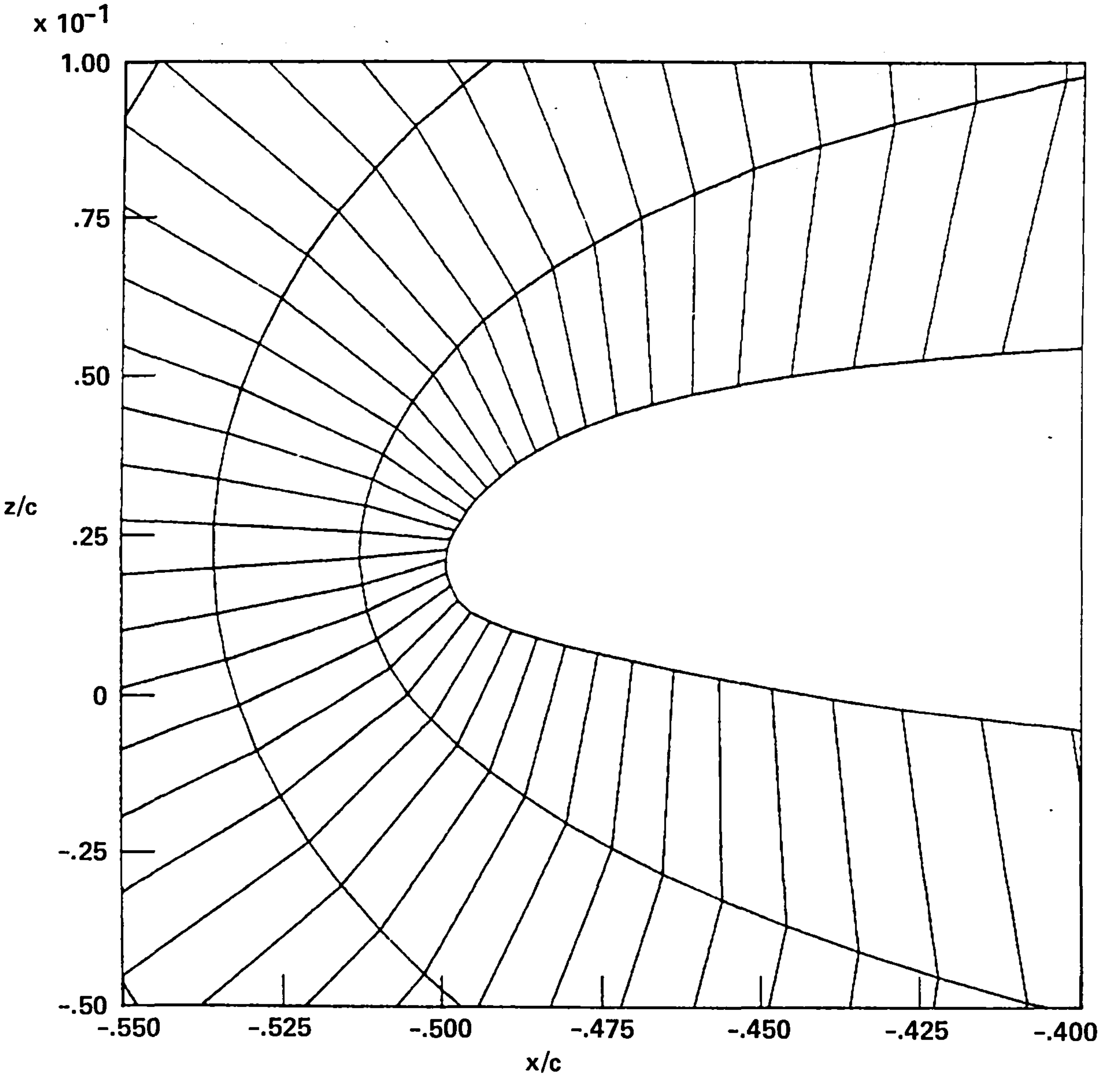
x 10⁻¹
1.00
.75
.50
z/c
.25
0
-.25
-.50
-.550
-.525
-.500
-.475
-.450
-.425
-.400
x/c

Figure 5.- Root station leading edge close up about configuration 4 (ref. 29).

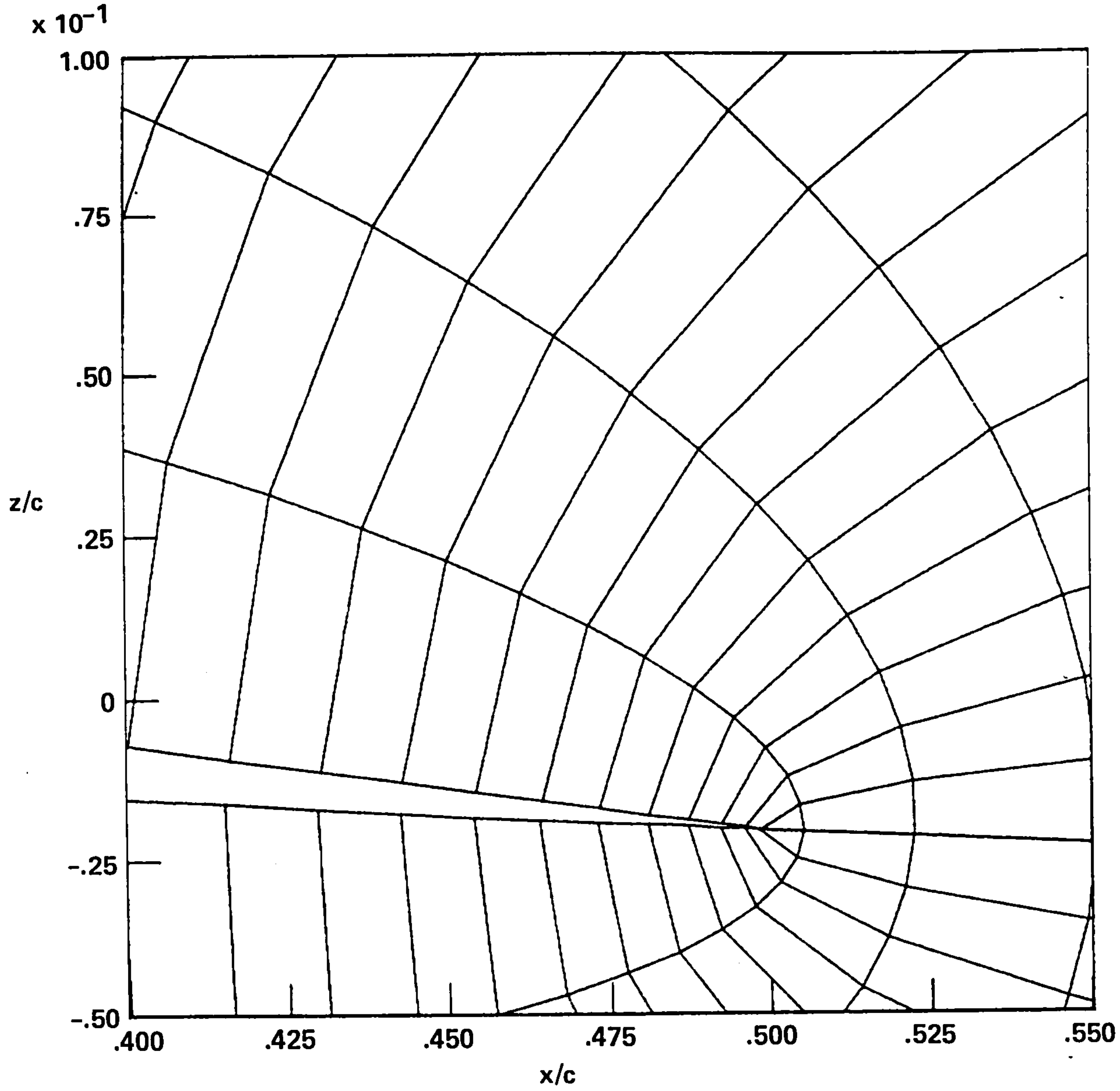

Figure 6.- Root station trailing edge close up about configuration 4 (ref. 29).

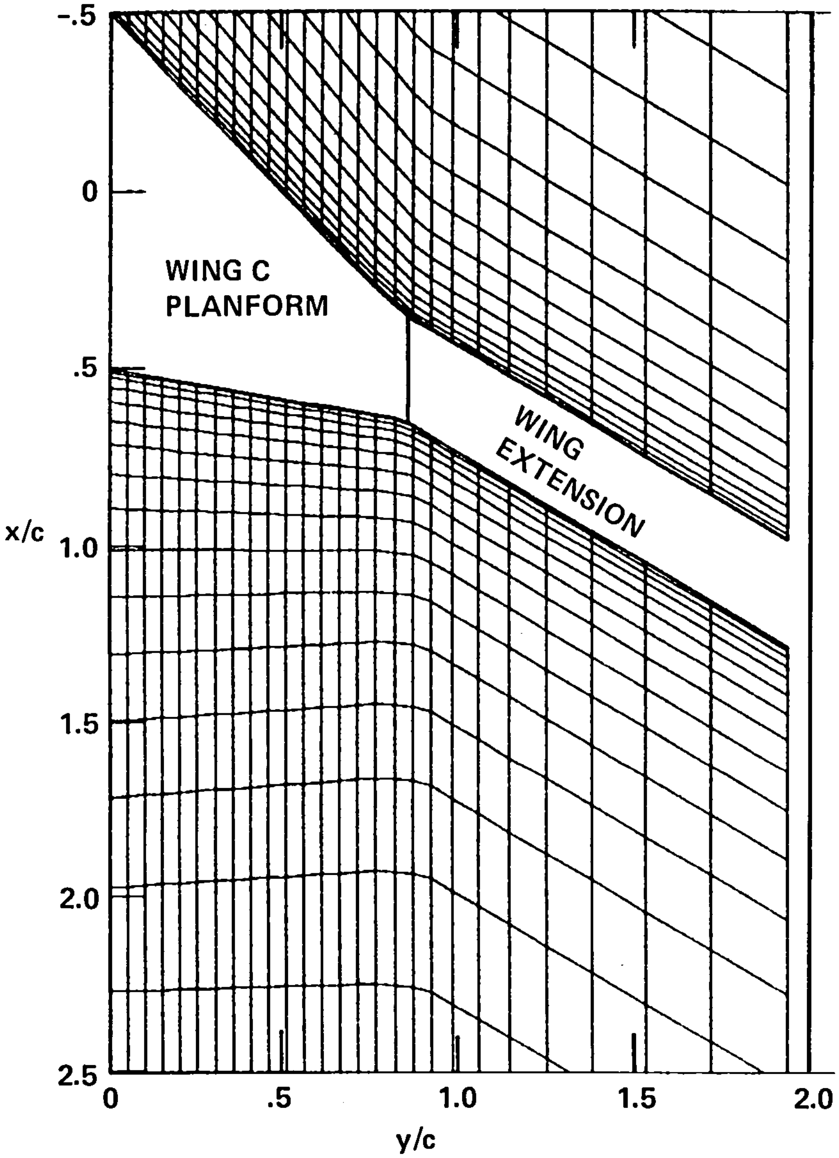
WING C
PLANFORM
WING
EXTENSION
-.5
0
.5
1.0
1.5
2.0
2.5
x/c
0
.5
1.0
1.5
2.0
y/c

Figure 7.- Three-dimensional grid about configuration 4 (ref. 29), planform view, 27×20 grid points.

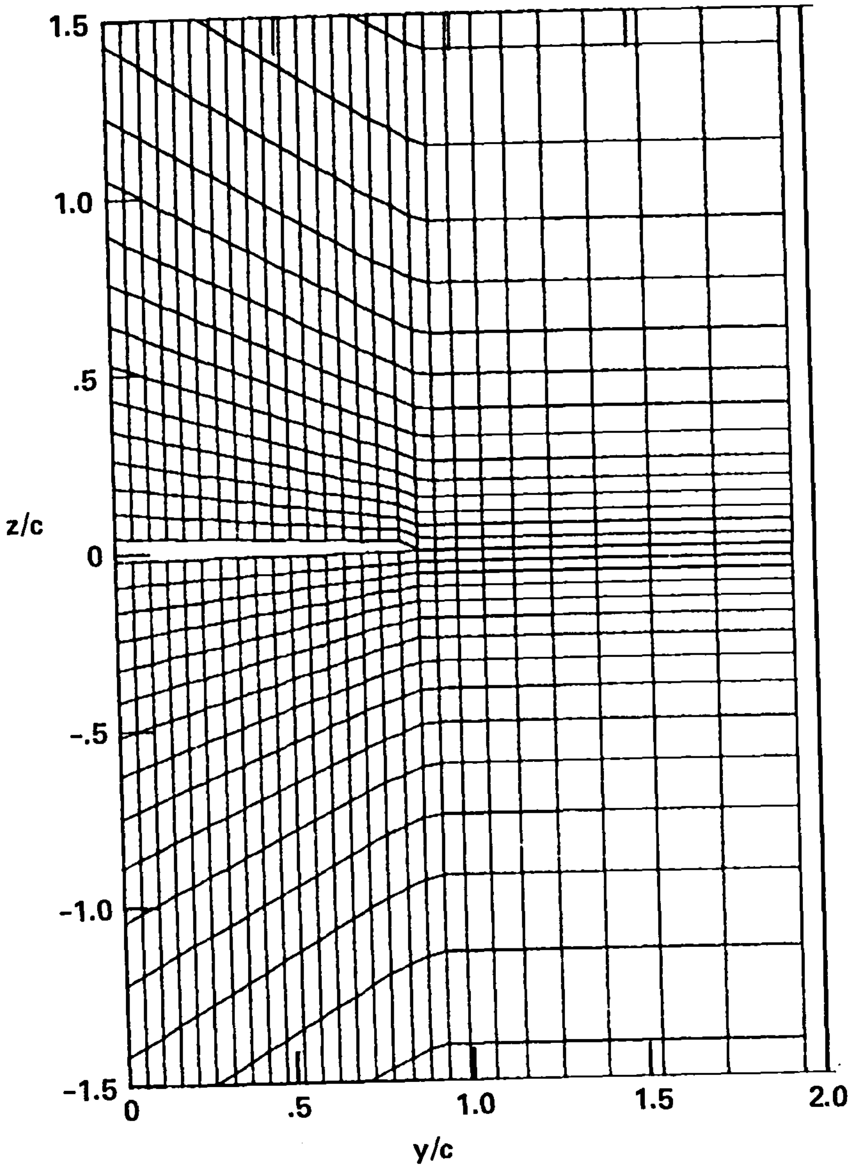
1.5
1.0
.5
z/c
0
-.5
-1.0
-1.5
0
.5
1.0
1.5
2.0
y/c

Figure 8.- Three-dimensional grid about configuration 4 (ref. 29), half chord view, 27×20 grid points.

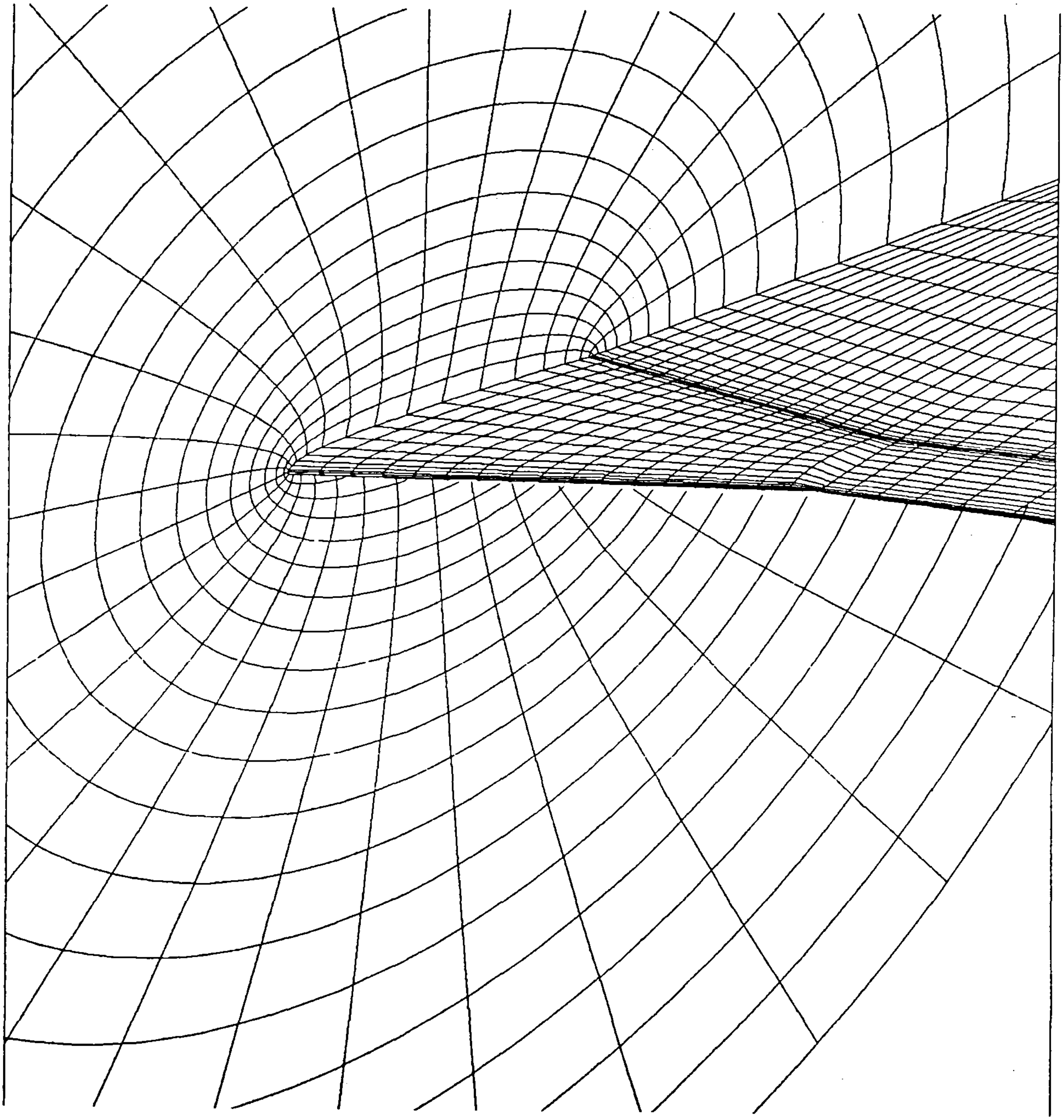

Figure 9.- Perspective view of the grid about configuration 4, 127×27×20 grid points, (only every fourth point plotted in the wraparound direction).

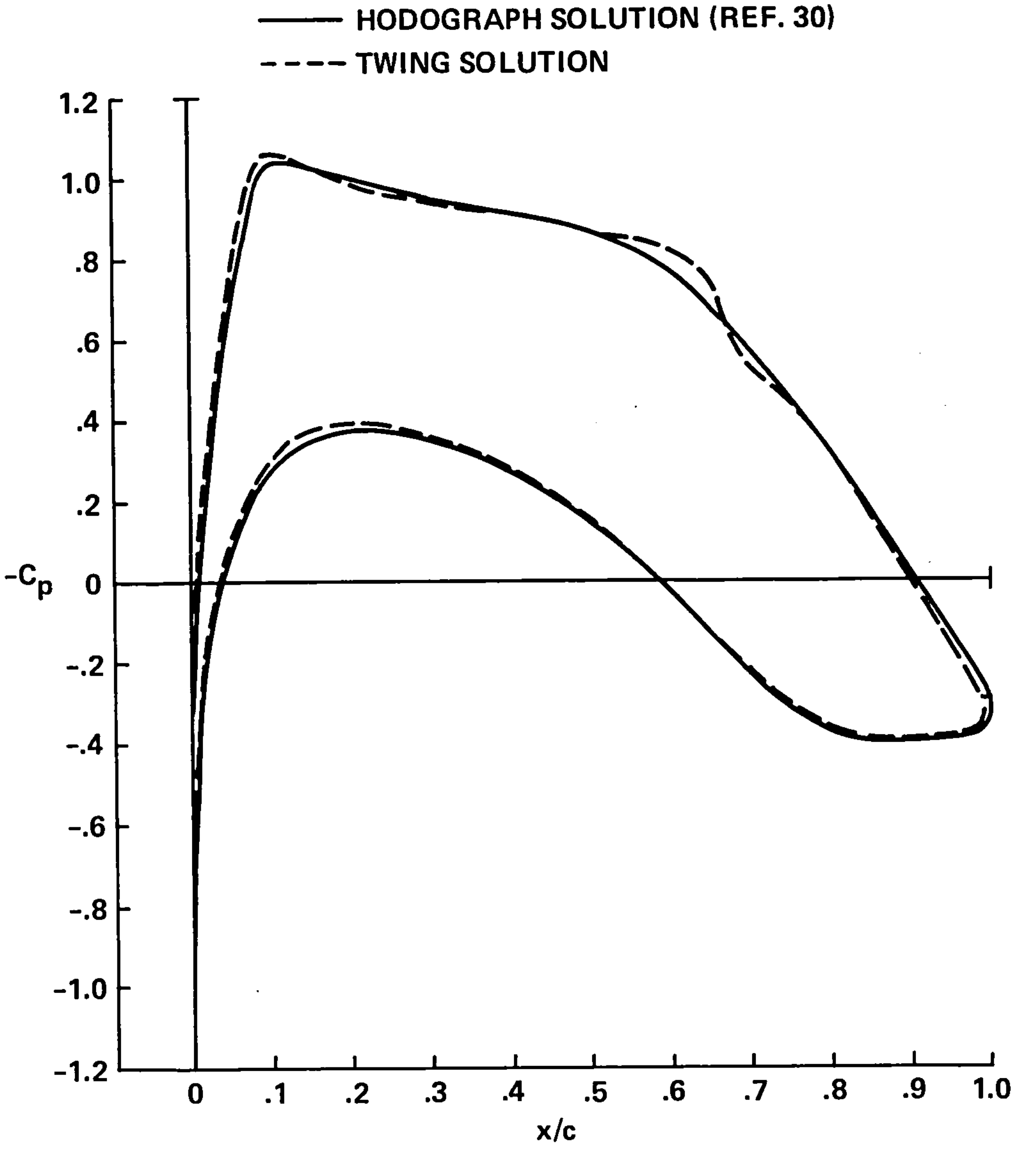

Figure 10.- Pressure coefficient comparison (airfoil 75-06-12, ref. 30, $M_\infty = 0.75$, $\alpha = 0.115°$).

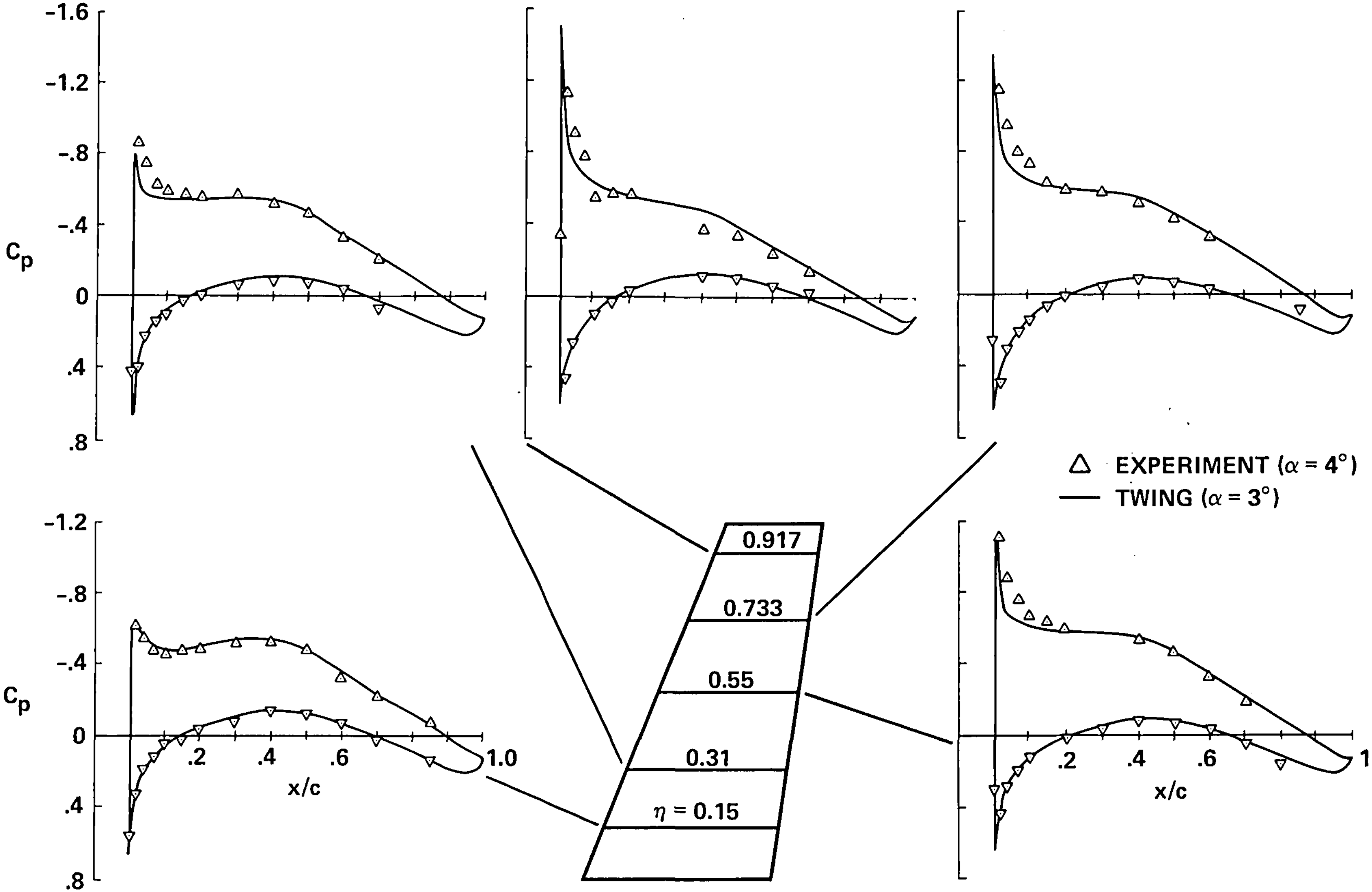

Figure 11.- Comparison of pressure coefficient distributions, configuration 1 (ref. 32), $M_\infty = 0.7$, $\Lambda_{LE} = 37.25°$, TR = 0.5, Æ = 6.0.

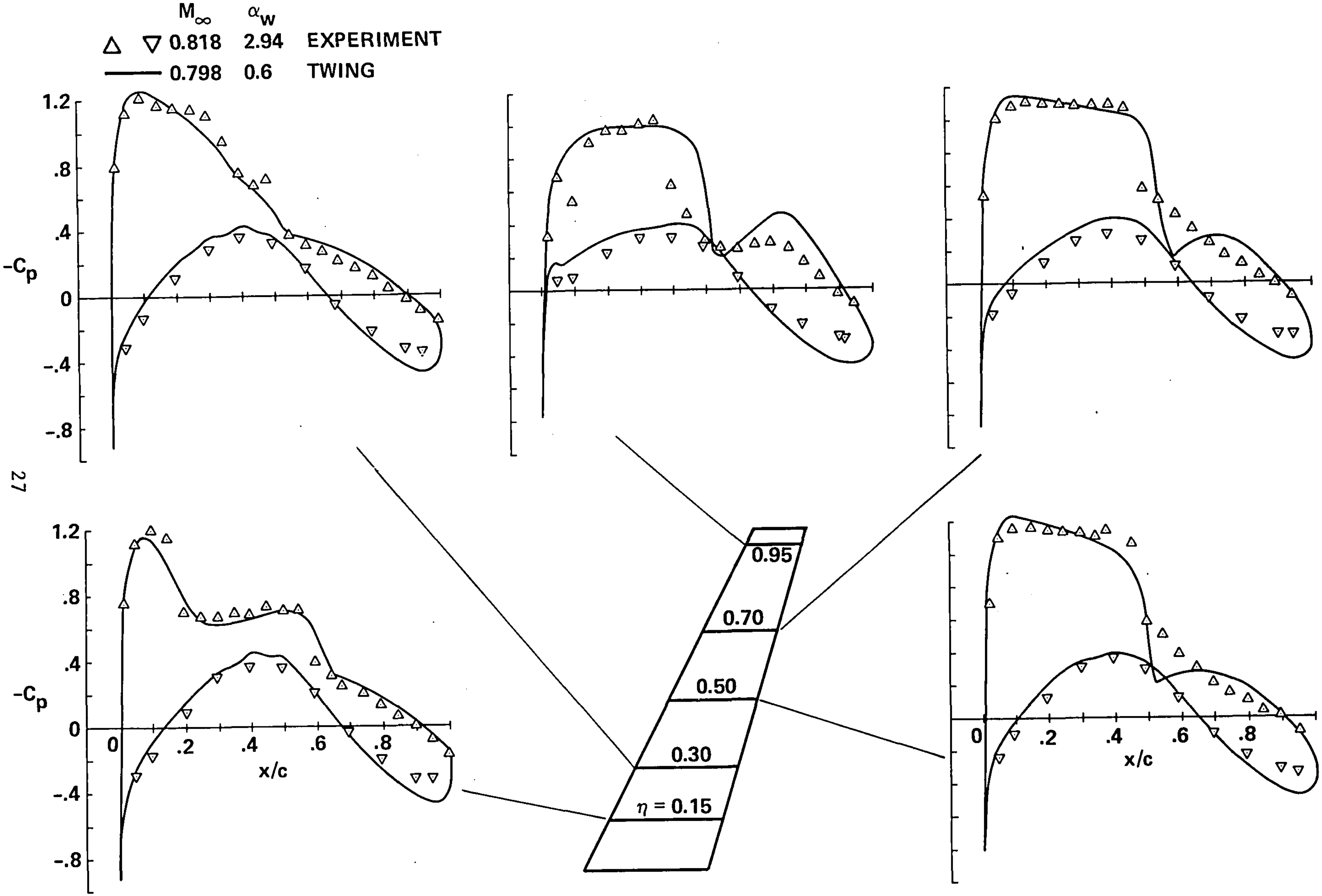

Figure 12.- Comparison of pressure coefficient distributions, experiment taken from Hinson and Burdges (ref. 29), configuration 2, $\Lambda_{LE}$ = 27°, TR = 0.4, Æ = 8.0.

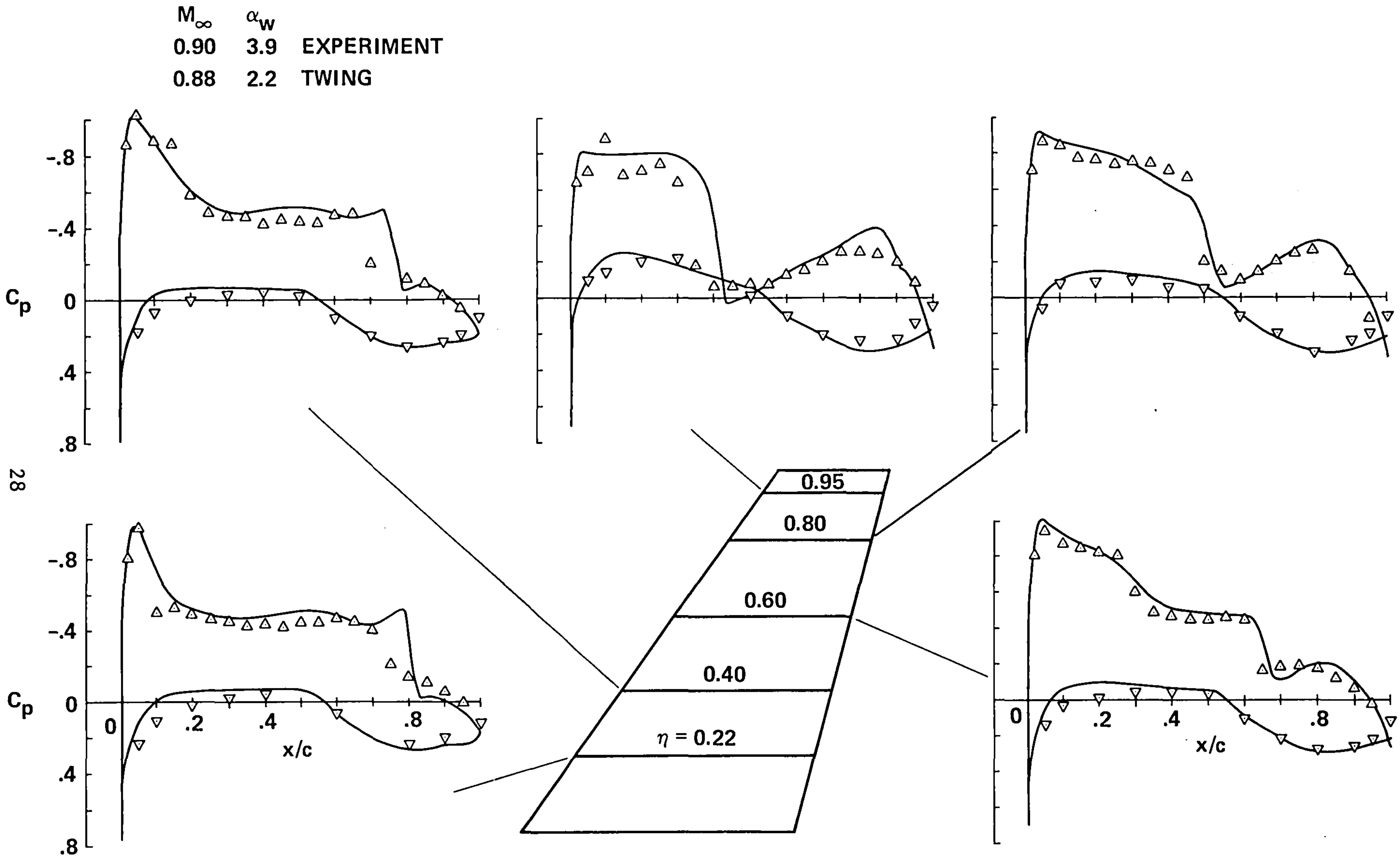

Figure 13.- Comparison of pressure coefficient distributions, experiment taken from Hinson and Burdges (ref. 29), configuration 3, $\Lambda_{LE}$ = 35°, TR = 0.4, Æ = 3.8.

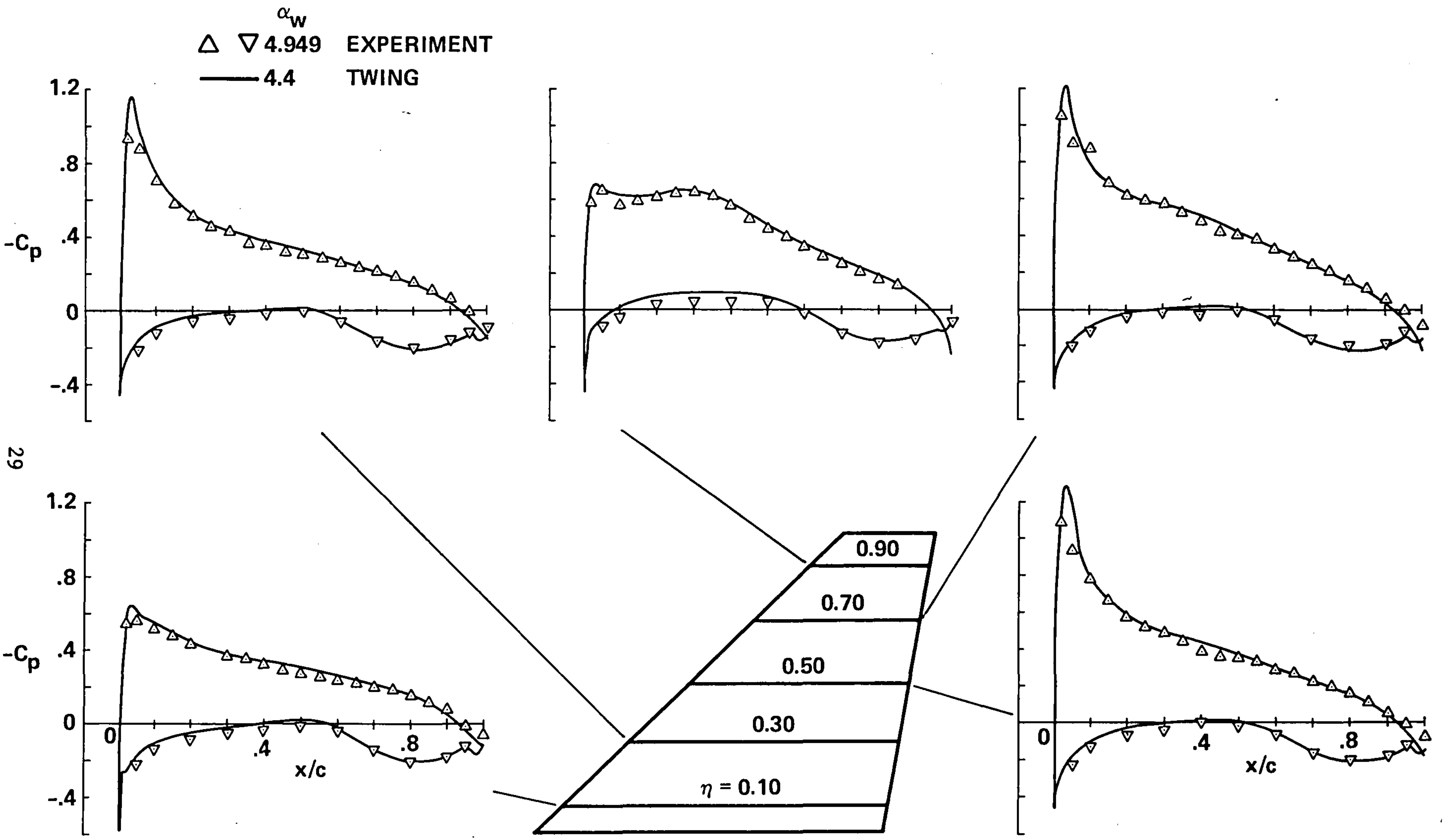

Figure 14.- Comparison of pressure coefficient distributions, experiment taken from Hinson and Burdges (ref. 29), configuration 4, $\Lambda_{LE} = 45°$, TR = 0.3, Æ = 2.6, $M_\infty = 0.7$.

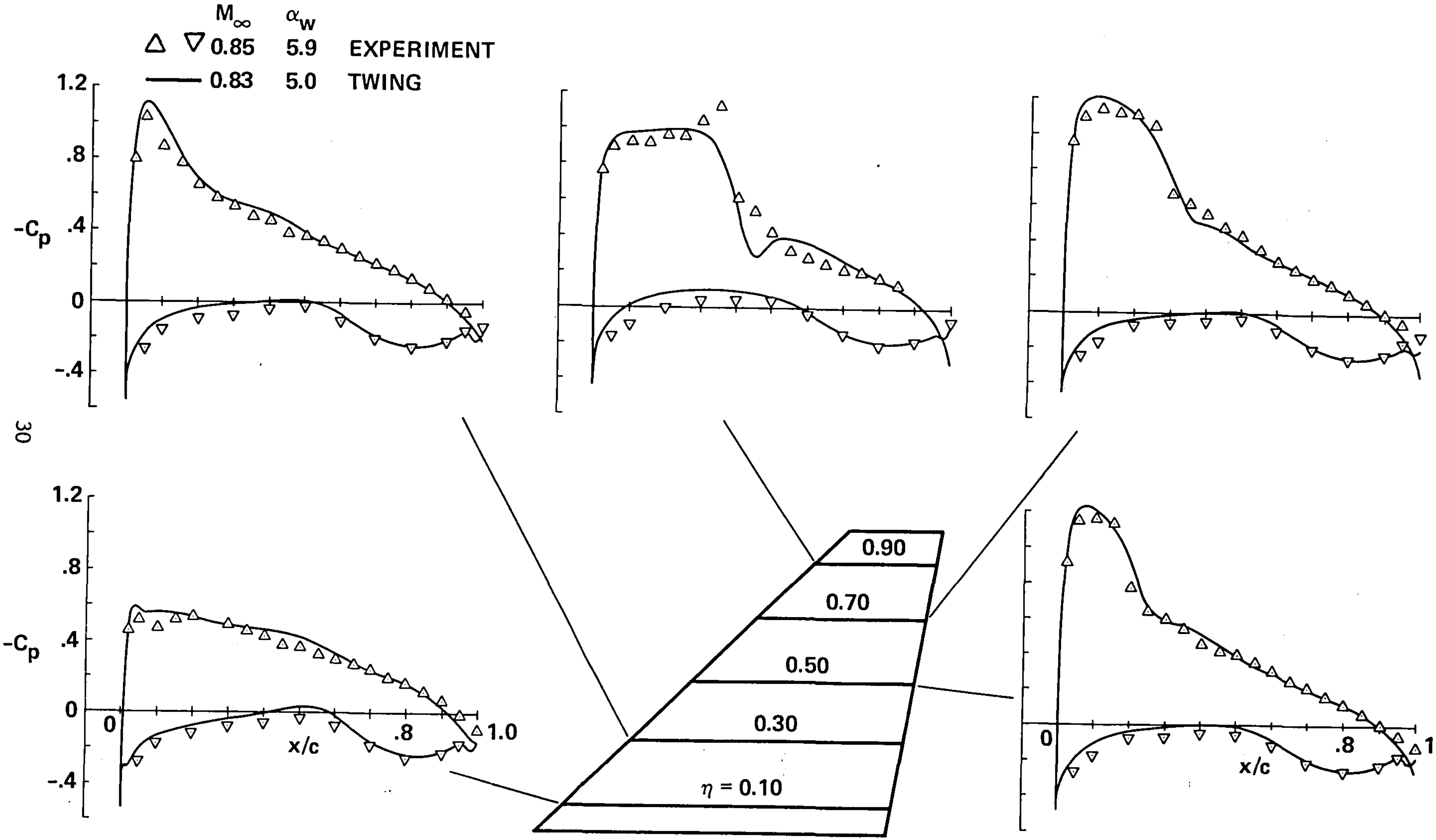

Figure 15.- Comparison of pressure coefficient distributions, experiment taken from Hinson and Burdges (ref. 29), configuration 4, $\Lambda_{LE}$ = 45°, TR = 0.3, Æ = 2.6.

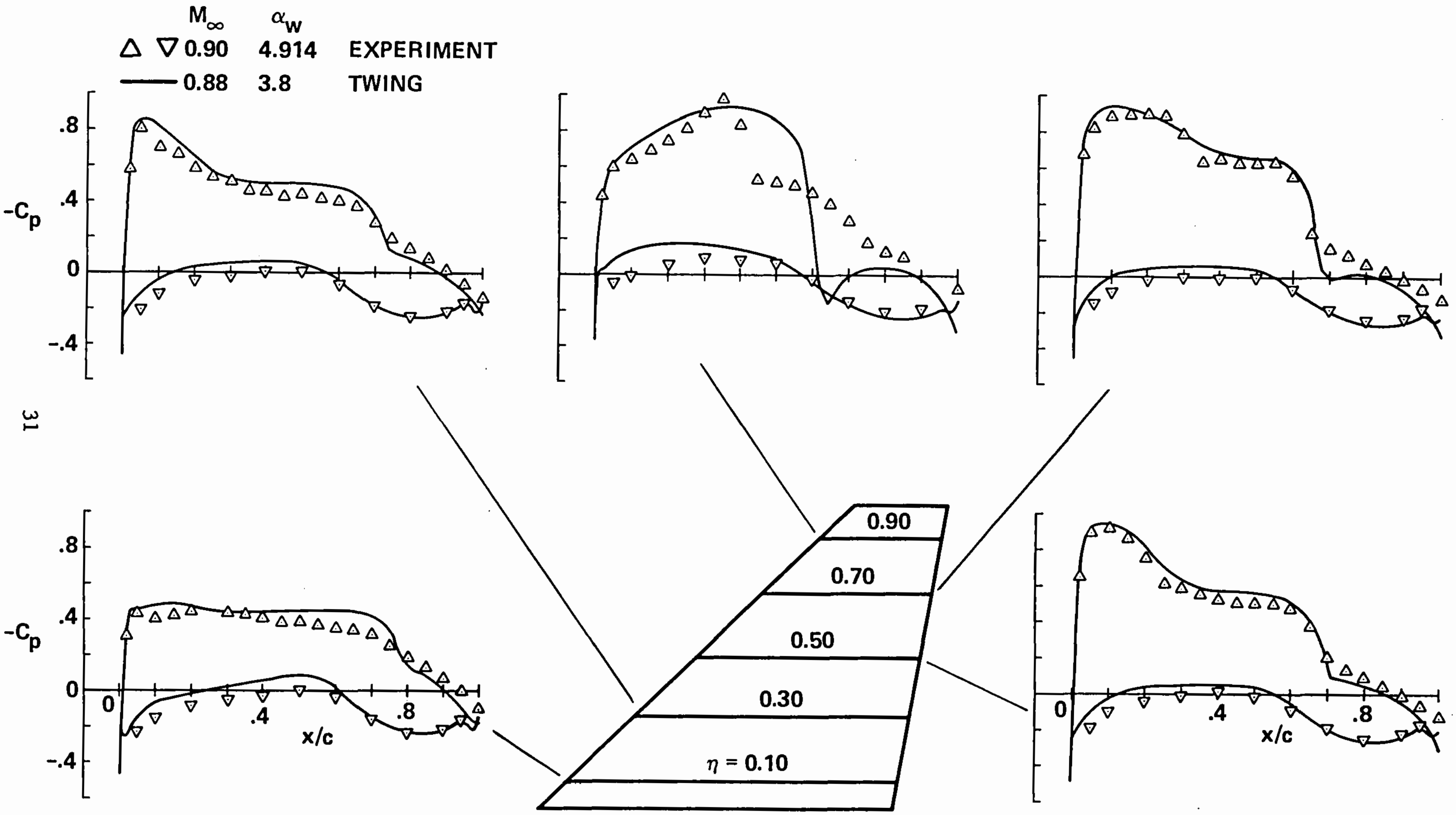

Figure 16.- Comparison of pressure coefficient distributions, experiment taken from Hinson and Burdges (ref. 29), configuration 4, $\Lambda_{LE}$ = 45°, TR = 0.3, Æ = 2.6.

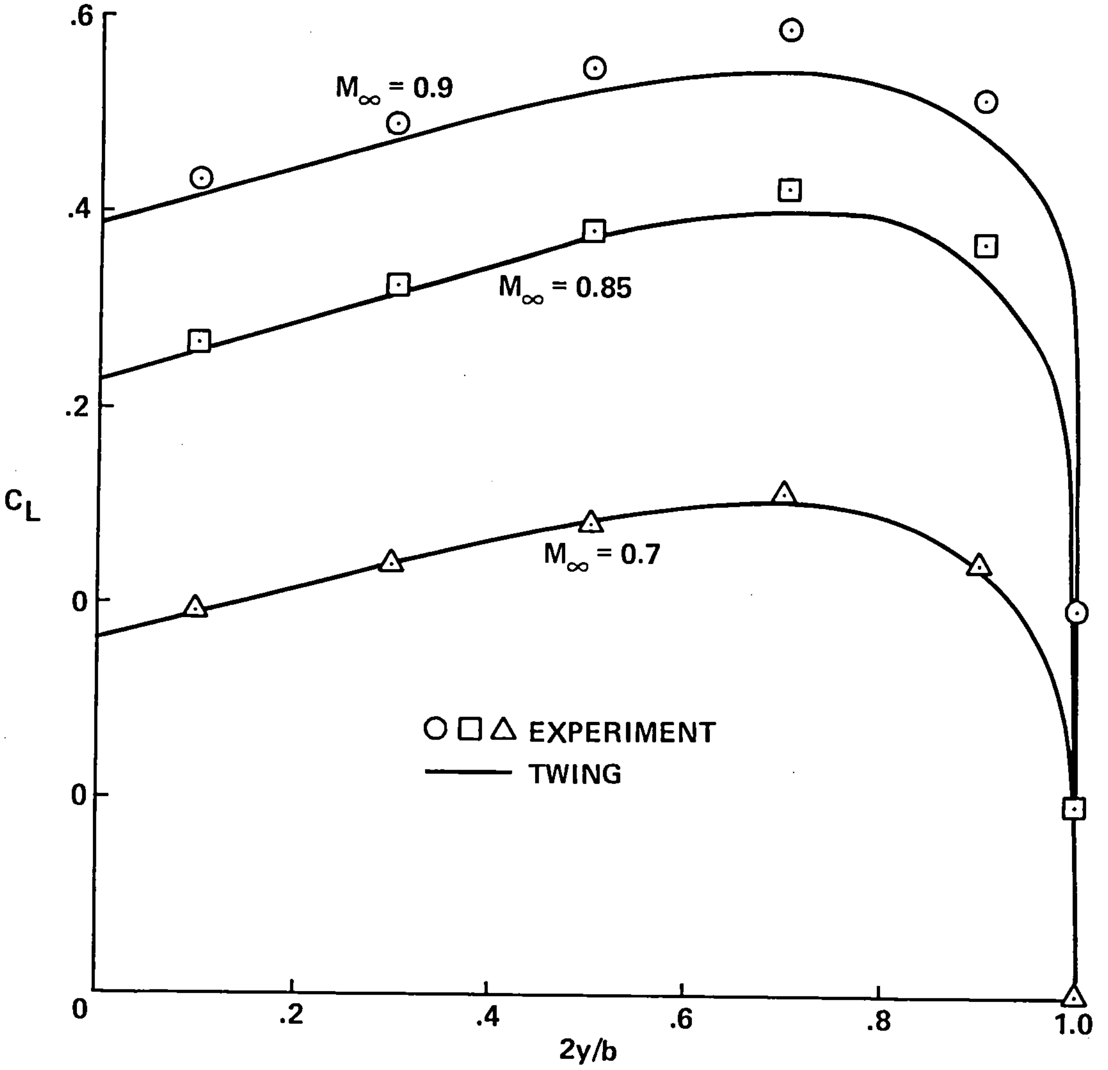

Figure 17.- Spanwise load distribution comparisons, configuration 4 (ref. 29).

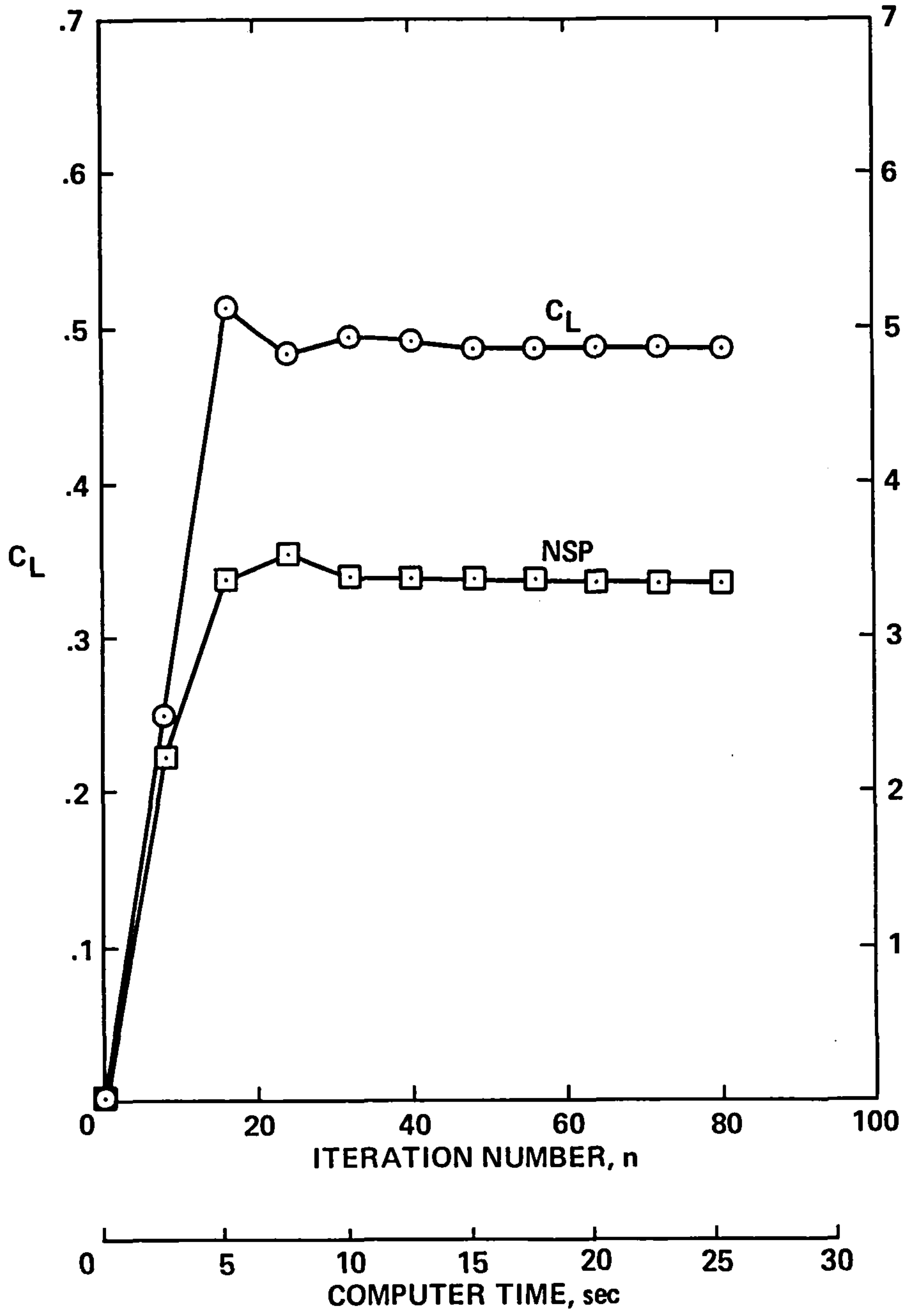

Figure 18.- Convergence characteristics of TWING, configuration 4, $M_\infty = 0.88$, $\alpha = 3.8°$.

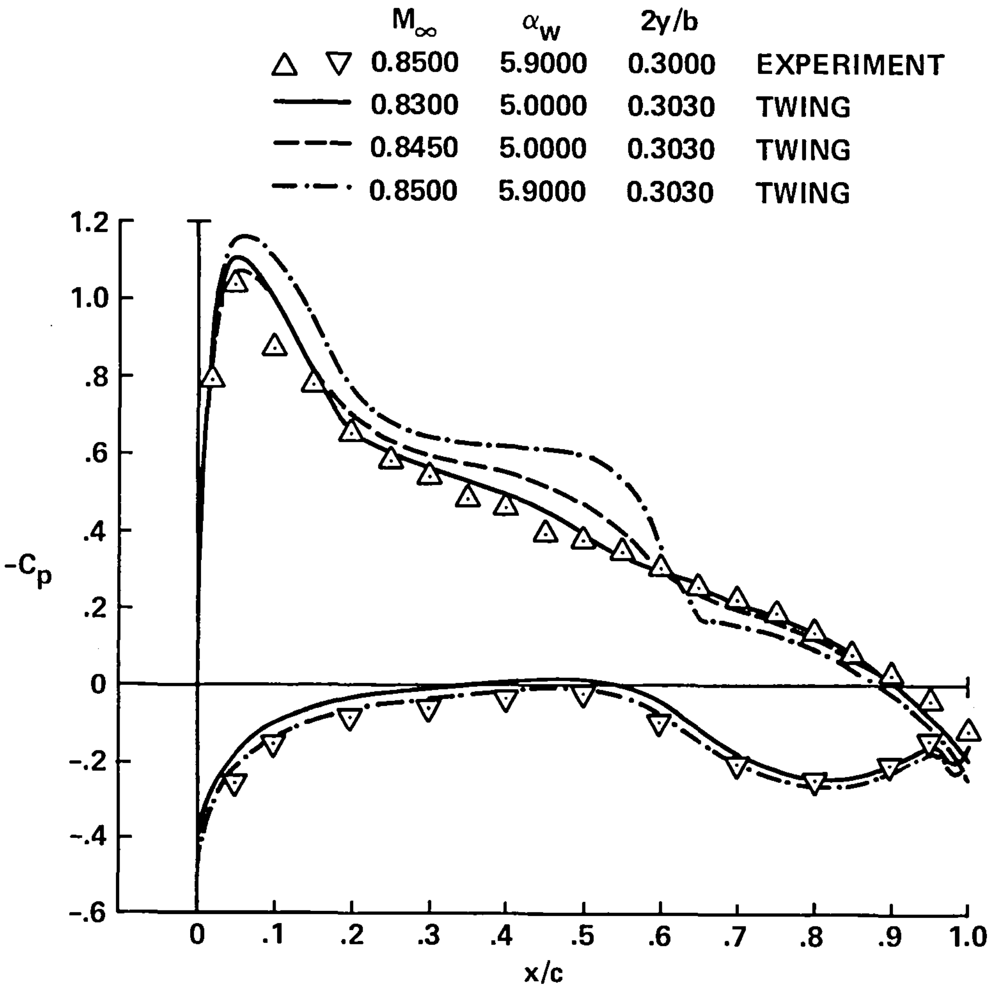

Figure 19.- Effect of Mach number and angle of attack corrections on the pressure coefficient distribution, experiment taken from reference 29, configuration 4, $\Lambda_{LE}$ = 45°, TR = 0.3, Æ = 2.6.

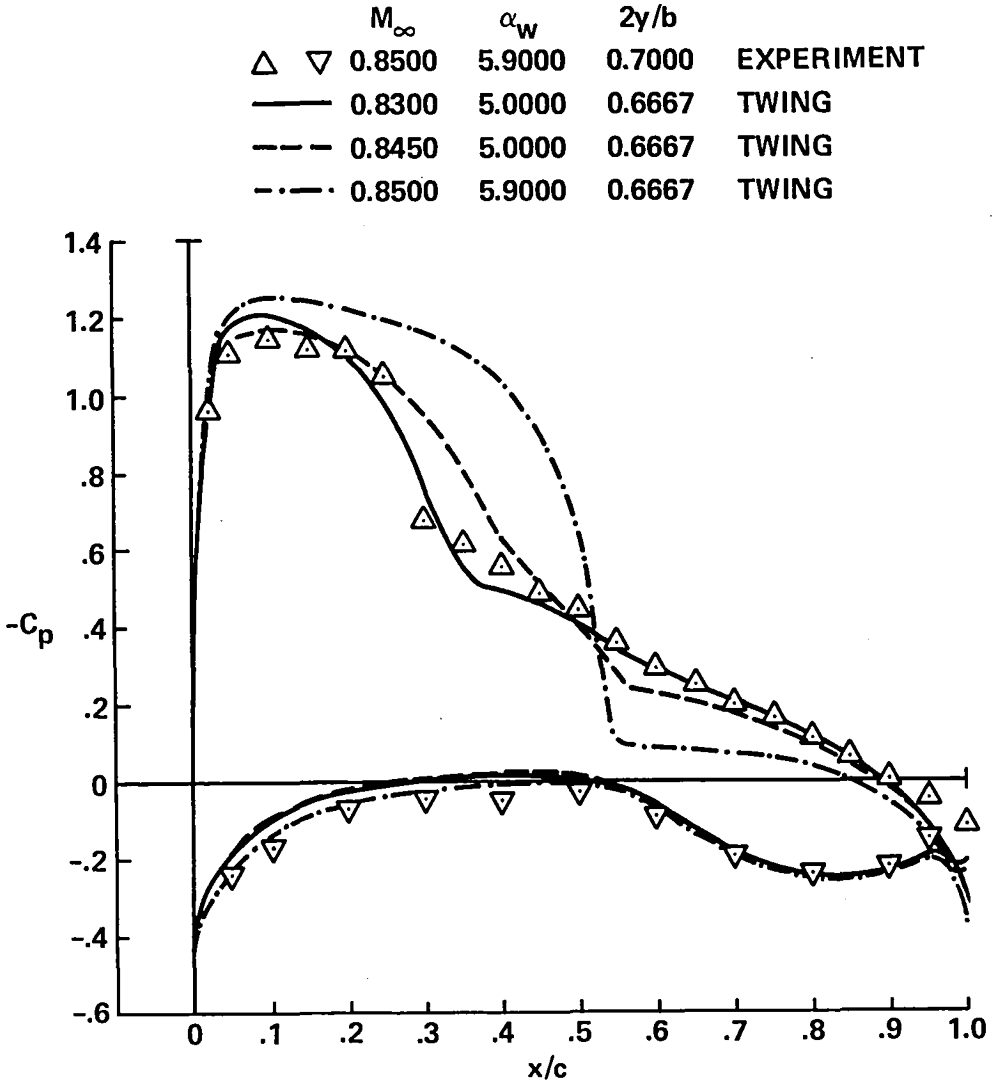

Figure 19.- Concluded.

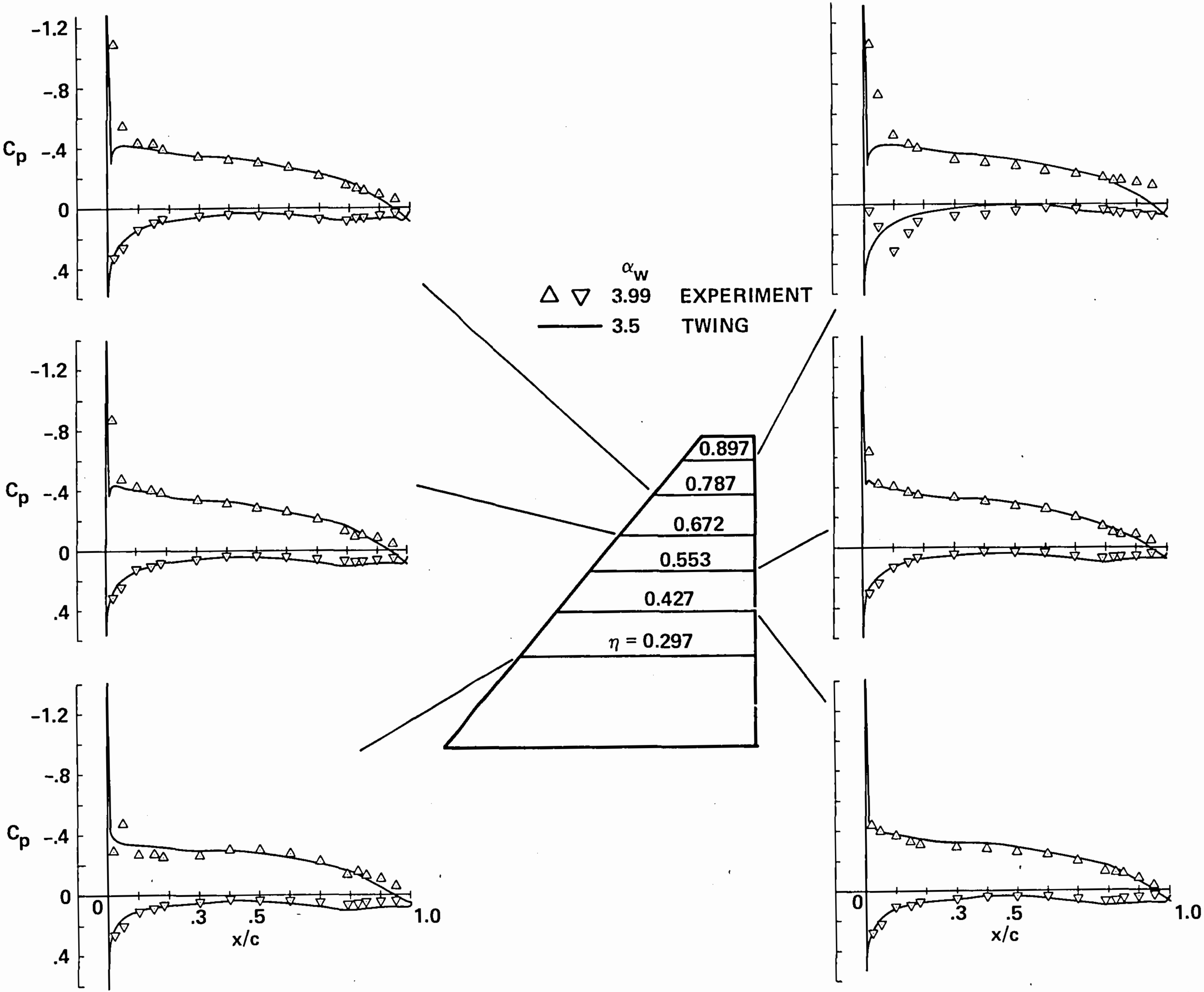

Figure 20.- Comparison of pressure coefficient distributions, experiment taken from R. Cox (private communication, 1982), configuration 5, $\Lambda_{LE}$ = 40°, TR = 0.177, $\mathcal{R}$ = 3.3, $M_\infty$ = 0.6.

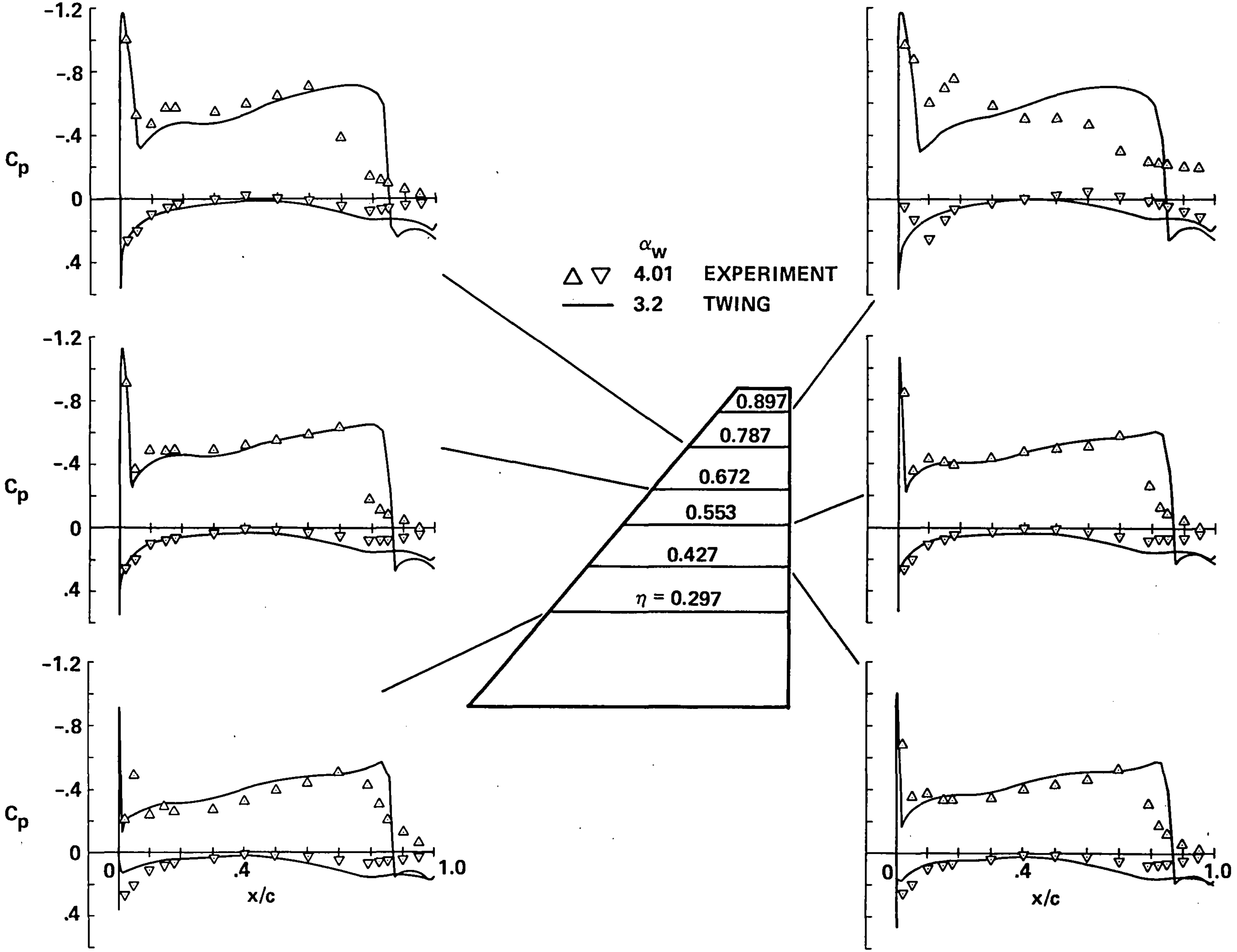

Figure 21.- Comparison of pressure coefficient distributions, experiment taken from R. Cox (private communication, 1982), configuration 5, $\Lambda_{LE}$ = 40°, TR = 0.177, $AR$ = 3.3, $M_\infty$ = 0.9.

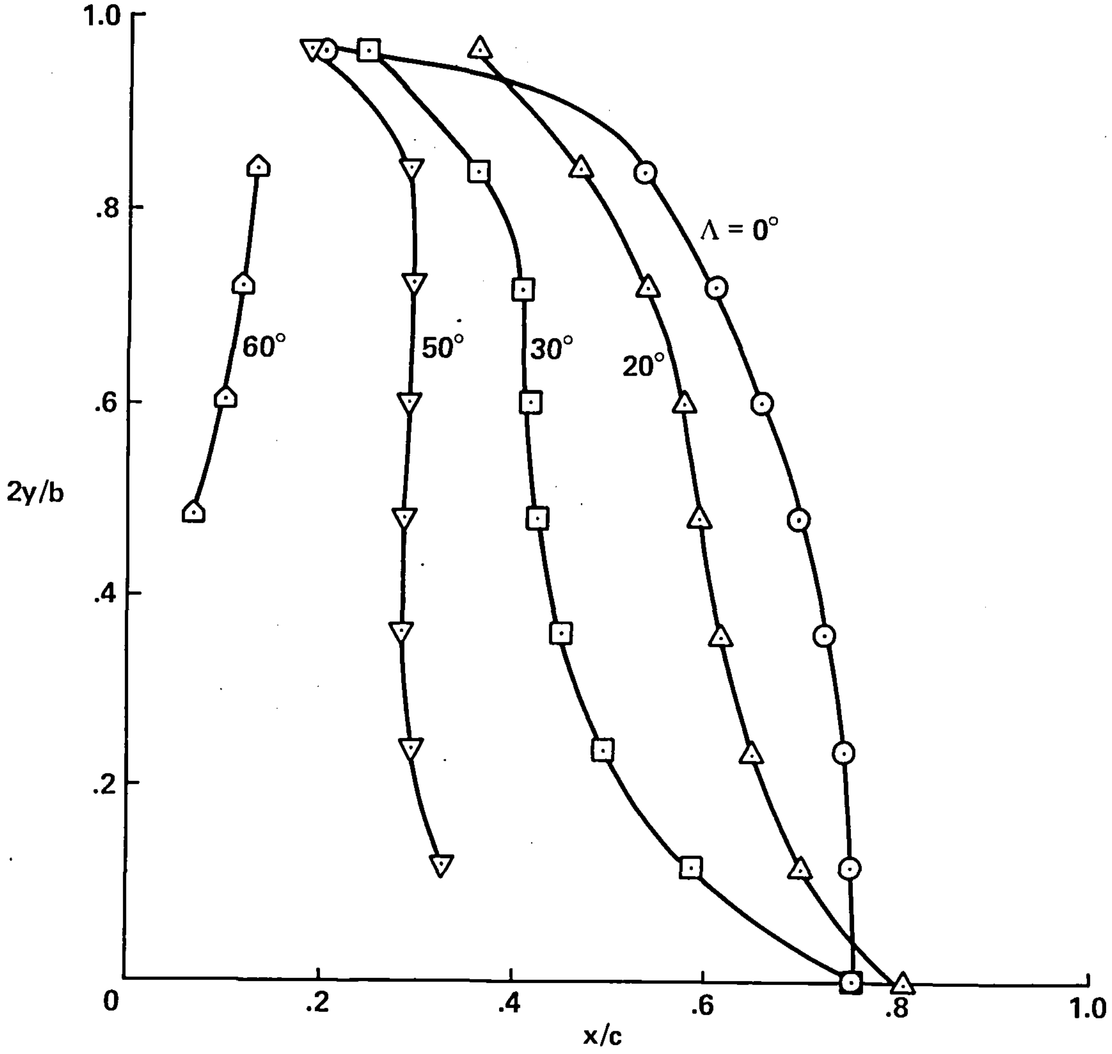

Figure 22.- Variation of shock sonic line with sweep, aft sweep (NACA 0012 airfoil sections, $M_\infty = 0.8$, $\alpha = 3°$, $A\!\!\!R = 6$, TR = 1.0).

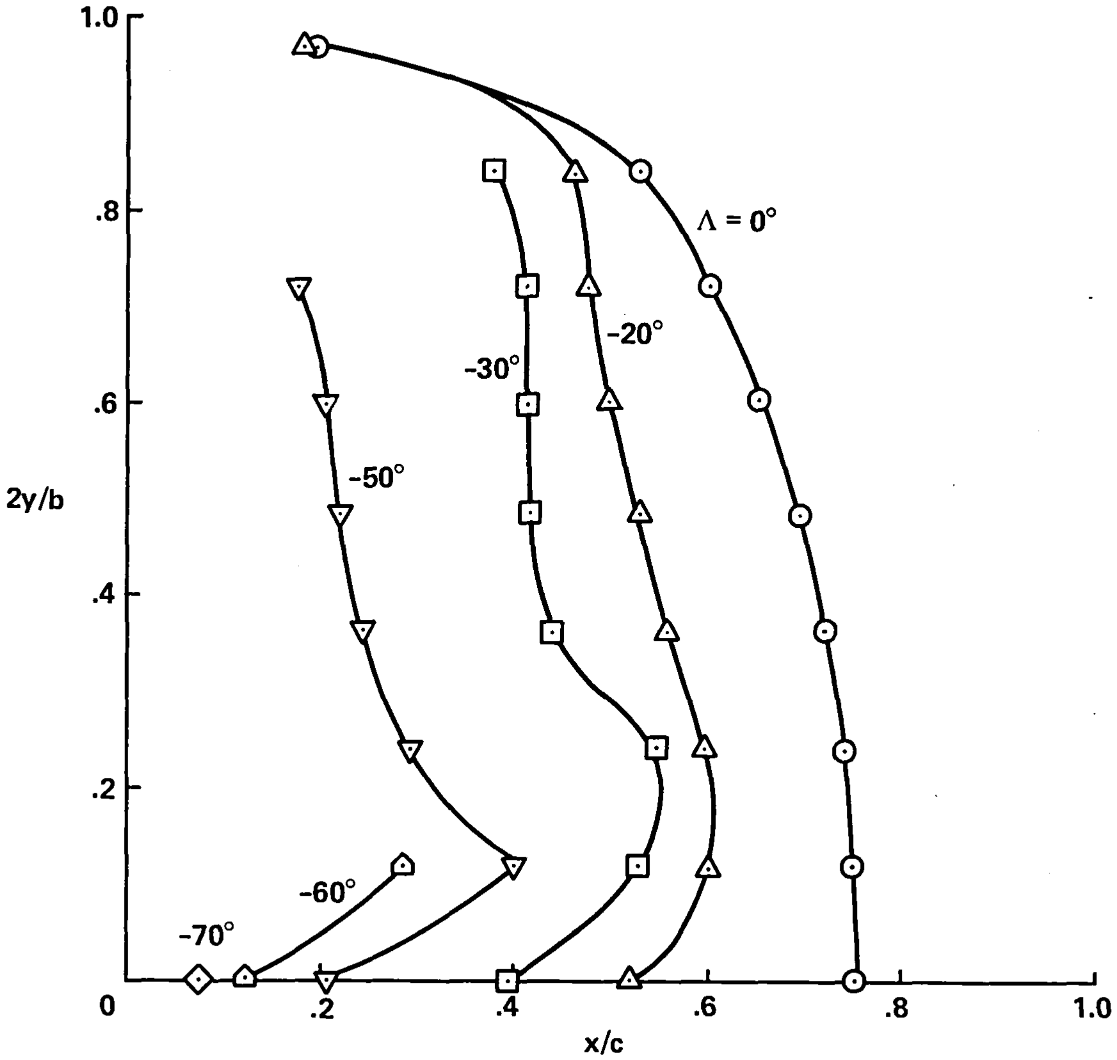

Figure 23.- Variation of the shock sonic line with sweep, forward sweep (NACA 0012 airfoil sections, $M_\infty = 0.8$, $\alpha = 3°$, $\mathcal{R} = 6$, TR = 1.0).

| | | |
|---|---|---|
| 1. Report No.<br>NASA TM-84283 | 2. Government Accession No. | 3. Recipient's Catalog No. |
| 4. Title and Subtitle<br>RECENT APPLICATIONS OF THE TRANSONIC WING ANALYSIS COMPUTER CODE TWING | | 5. Report Date<br>August 1982<br>6. Performing Organization Code |
| 7. Author(s)<br>N. R. Subramanian, Terry L. Holst, and Scott D. Thomas | | 8. Performing Organization Report No.<br>A-9035 |
| 9. Performing Organization Name and Address<br>NASA Ames Research Center<br>Moffett Field, Calif. 94035 | | 10. Work Unit No.<br>T-9682<br>11. Contract or Grant No. |
| 12. Sponsoring Agency Name and Address<br>National Aeronautics and Space Administration<br>Washington, D.C. 20546 | | 13. Type of Report and Period Covered<br>Technical Memorandum<br>14. Sponsoring Agency Code<br>505-31-11 |

15. Supplementary Notes

Point of Contact: Terry L. Holst, Ames Research Center, MS202A-14,
Moffett Field, CA 94035. (415) 965-6415 or FTS 448-6415

16. Abstract

This report presents an evaluation of the transonic-wing-analysis computer code TWING. TWING utilizes a fully implicit approximate factorization iteration scheme to solve the full potential equation in conservative form. A numerical elliptic-solver grid-generation scheme is used to generate the required finite-difference mesh. Several wing configurations have been analyzed, and the limits of applicability of this code have been evaluated. Comparisons of computed results have been made with available experimental data. Results indicate that the code is robust, accurate (when significant viscous effects are not present), and efficient. TWING generally produces solutions an order of magnitude faster than other conservative full potential codes using successive-line overrelaxation. The present method is applicable to a wide range of isolated wing configurations including high-aspect-ratio transport wings and low-aspect-ratio, high-sweep, fighter configurations.

| | | | |
|---|---|---|---|
| 17. Key Words (Suggested by Author(s))<br>Transonic Flow<br>Numerical Methods | | 18. Distribution Statement<br>Unlimited<br>Subject Category 02 | |
| 19. Security Classif. (of this report)<br>Unclassified | 20. Security Classif. (of this page)<br>Unclassified | 21. No. of Pages<br>42 | 22. Price*<br>A03 |

*For sale by the National Technical Information Service, Springfield, Virginia 22161

LANGLEY RESEARCH CENTER
3 1176 00505 2031